Top Catal (2016) 59:420–438
DOI 10.1007/s11244-015-0534-2

ORIGINAL PAPER

Ambient Pressure X-ray Photoelectron Spectroscopy for Probing Monometallic, Bimetallic and Oxide-Metal Catalysts Under Reactive Atmospheres and Catalytic Reaction Conditions

Selim Alayoglu[1] · **Gabor A. Somorjai**[1]

Published online: 30 December 2015

Abstract Synchrotron-based ambient pressure X-ray photoelectron spectroscopy (APXPS) is an important in situ chemical probe in the toolbox of chemists and materials engineers. It uniquely aids in the investigation of the surfaces and interfaces of complex systems under dynamic environments, such as catalysts operating at the solid/gas interface. Nanoparticles (NPs) produced via colloidal chemistry offer the advantage of narrow particle distributions in APXPS studies of catalysts. They provide a narrow distribution in size, shape and composition of catalysts, which provide a closer correlation to actual catalysts than single crystal models for which APXPS is extensively employed. In this paper, some case studies of colloidaly-made uniform nanoparticles catalysts will be outlined. The examples will include monometallic, bimetallic and binary oxide-metal catalysts, where APXPS is used in different reactive atmospheres and during catalytic reactions. First, in situ CO oxidation studies of monometallic Rh NPs in the 2–7 nm range will be discussed. Next, APXPS studies of bimetallic NPs with size and composition control will be illustrated. NO-induced reversible core/shell restructuring of bimetallic PdRh NPs and gas-driven irreversible surface segregation of Cu in bimetallic CoCu NPs will be explained. To further illustrate the utility of the technique, APXPS and catalytic measurements carried out in parallel and under identical conditions will be described over bimetallic AuPd and CoPt NPs, during catalytic oxidation of CO. APXPS based structure–function correlations such as composition and ensemble dependence of catalytic activity will also be illustrated in this discussion. Finally, binary oxide-metal catalysts will be exemplified in APXPS studies of CeO_2/Pt and TiO_2/Co systems in hydrogen reducing atmospheres and/or during catalytic hydrogenation of CO_2. Also, along with this idea, metal-support interactions in the forms of metal-induced reduction of oxide support, wetting and encapsulation of metal will be detailed in relation to catalytic properties.

Keywords Ambient pressure X-ray photoelectron spectroscopy · Nanoparticles · Catalyst · Bimetallic · Oxide–metal interface

1 Introduction

X-ray photoelectron spectroscopy (XPS) is widely employed for elemental characterization, chemical speciation and composition analysis of naturally occurring or engineered materials. Laboratory use of XPS is limited to a number of fixed or rotating anode X-ray sources such as Al Kα and Mg Kα [1], although synchrotron facilities around the world offer monochromatic and tunable photon energies at high fluxes. XPS is an ultra-high vacuum (UHV) technique, due to the short mean free path (MFP) of photoelectrons in matter (either gas or condensed phases). Strictly defined by analyzer design and its instrumental execution, photoelectrons ejected from core levels have to travel in space (i.e. UHV) long distances in comparison with electron MFPs in any gas pressure. In situ XPS, which was first realized using laboratory X-ray sources in the 1970s [2], overcame the problem of gas pressure by using an ambient pressure cell (i.e. vacuum chamber) separated from the analyzer, yet connected via a small aperture cone

✉ Selim Alayoglu
salayoglu@lbl.gov

[1] Chemical Sciences Division, Lawrence Berkeley National Laboratory and Department of Chemistry, University of California, Berkeley, USA

and differentially pumped stages. The first generation synchrotron-based in situ XPS happened to be known as ambient pressure XPS (APXPS), where ambient pressure is broadly defined as pressures at and above 10 milliTorr [3]. APXPS now exists in over 10 synchrotron facilities around the world and is also sold commercially.

APXPS has opened many new research possibilities in surface science and catalysis [4]. Studies of single crystal surfaces are usually limited to high vacuum conditions ($<10^{-7}$ Torr), where reaction probabilities are extremely low, while realistic catalysts operate at atmospheric pressures (15–76,000 Torr). Ambient pressure cells in APXPS can be dosed with reactive gases (H_2, O_2, H_2O, CO, NO, etc.) up to $\sim$5 Torr, and therefore XPS measurements can be performed in catalytically relevant gas pressures. By this way, APXPS helped closing this pressure gap in catalysis. In only the brief 10 year history of synchrotron APXPS, the technique has revolutionized the fields of surface, interface, colloid and catalysis science. For example, thermochemical fluctuations in electronic and redox properties can now be monitored for near surface alloy catalysts under reactive gas atmospheres and at elevated temperatures [5, 6]; or real-time ad-layer formation and adsorbate-induced clustering of single crystals can now be understood in combination with microscopy (e.g. high pressure scanning tunneling microscopy) [7]. It has also made way for new possibilities in materials screening where chemical and electronic structures of engineered nanomaterials such as catalysts, sensors and membranes can be interrogated under relevant environments. Even working fuel cell environments have been created in APXPS chambers, which has led to in situ investigation of electrocatalyst films as electrons and ions are transferred across [8].

Catalysts employed in realistic industrial applications are nanomaterials with non-uniform surface properties. However, bulk materials with well-controlled surface properties (e.g. single crystal surfaces) were in the focus of surface science and catalysis in the past century. In an attempt to overcome this long-existing materials gap in catalysis, bulk single crystal and polycrystalline films gave way to two-dimensional nanoparticles with well-defined structures at the atomic level [9–13] (Scheme 1). Because colloidal chemistry allows synthesis of low dimensional nano-structures with well-controlled physical and chemical properties, many researchers adopted colloidal synthetic techniques and strategies. By this way, size-, shape- and composition-controlled nanoparticles were produced; and their structure dependent catalytic behavior were studied for a number of processes such as oxidation of CO [14–16], ethylene epoxidation [17], hydrogenative isomerization of hydrocarbons [18–20], coupling reactions [21] and hydrogenation of molecules like CO [22, 23], CO_2 [24], furans [25, 26], pyrroles [27], alkynols [28] and benzene [29, 30]. This systematic work uncovered structure-sensitive catalytic behavior and trends for transition metal catalysts like Pt, Rh, Pd, Ru and Co. Also in these studies, sum frequency generation (SFG) vibrational spectroscopy was employed as an in situ surface probe with detection sensitivity at sub monolayer coverage. Combined with the catalytic reactor measurements, SFG provided the microstructure of the surface ad-layer for single crystals and nanoparticle films alike, in the form of adsorbate orientation and binding geometry [31].

It is necessary to comment on the role of capping agent that is often employed to protect colloidal nanoparticles. Although there are strategies established to remove capping agents, thermal treatment in O_2 [32], UV/ozone treatment [33, 34], refluxing in water [35], O_2 plasma cleaning, etc. it is often for the better to leave colloidal nanoparticles as-synthesized. Because heat and reactive O_2 gas or plasma used in such procedures are sometimes capable of altering the size, shape, morphology or composition of nanoparticles [32, 36], the very factors unique to colloidal synthesis. Furthermore, polymeric capping agents like polyvinylpyrrolidone (PVP), which is usually utilized in our work, weakly interact with nanoparticle surfaces and have shown to not interfere with catalytic activity and/or selectivity in the solid–gas interface. This was demonstrated on Pt surfaces during hydrogenation of furans [25] using combined SFG and catalytic measurements. Partial activity losses observed for other catalytic reactions were often attributed to the loss of available surface due to blockage [18], and no geometric or electronic effect of capping agents has been reported to date. However, it should be noted that phosphorous containing capping agents like trioctyl phosphine were inhibitory towards hydrogenation of CO_2 due to possibly a surface ensemble effect [24, 37]. Likewise, thiol-stabilized Pt and AuPt NPs were demonstrated to exhibit promotional effects during hydro-desulfurization reaction [38]. For this, we have avoided the use of phosphorous by developing alternative synthetic procedures when possible as illustrated for oleicacid capped Co NPs in our hydrogenation of CO_2 [24].

APXPS has transformed our in situ capabilities from probing the vibrational configuration of the topmost surfaces to monitoring chemically and electronically the near surface region. Coupled to catalytic reactor measurements, carried out in parallel, APXPS took our understanding of metal catalysts a step forward into the atomic level (Scheme 1). This review will discuss case examples of our APXPS studies combined with other techniques such as transmission electron microscopy (TEM) and in situ X-ray absorption spectroscopy (XAS). First, the case of monometallic catalysts will be illustrated where size-controlled Rh NPs were characterized with APXPS during catalytic oxidation of CO. Next, bimetallic systems will be

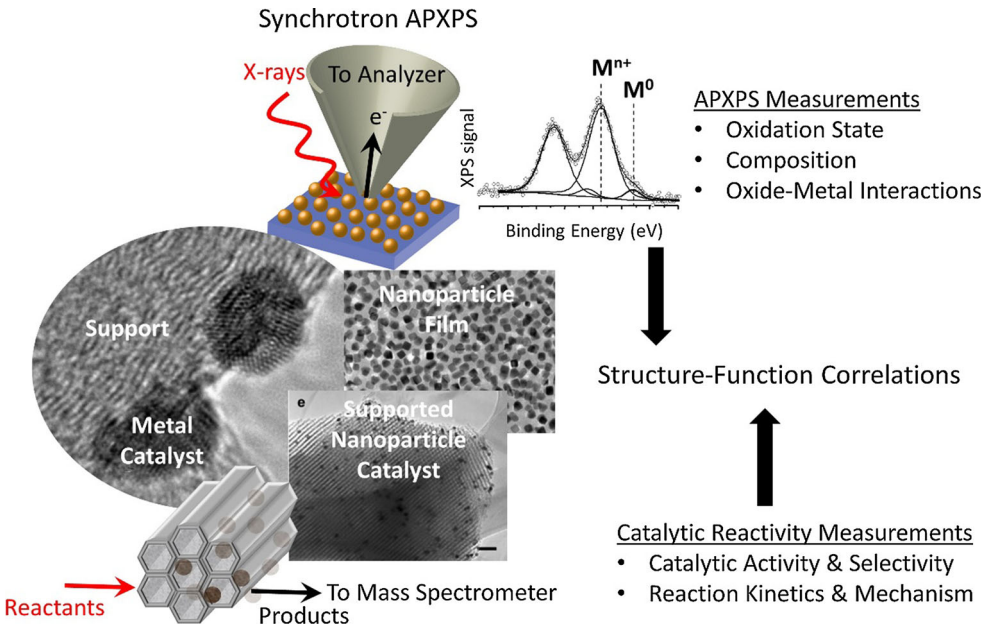

Scheme 1 Combined synchrotron APXPS & catalytic reactivity measurements for colloidal NP catalysts

discussed, focusing on composition-controlled bimetallic NPs of PdRh, CoCu, AuPd and CoPt, examined under reactive gas atmospheres or CO + O_2 reaction conditions using APXPS. Reversible restructuring of bimetallic PdRh NPs and irreversible segregation of bimetallic CoCu NPs will be first illustrated. Composition-activity correlations will then be explained over bimetallic AuPd and CoPt NPs. Finally, two binary oxide-metal catalysts, CeO_2/Pt and TiO_2/Co will be shown as exemplary cases of APXPS probing of metal-support interactions.

2 APXPS Studies on Monometallic NP Catalysts

It is often true that catalytic behavior of nanoparticles is governed by their structural properties at the molecular level. For monometallic nanoparticles, catalysts in the simplest configurational form, the relevant molecular factors are particle size and crystallographic shape, which are both strongly correlated. Particle size indirectly determines oxidizability (or reducibility) of the metal in reactive atmospheres [39], and also the coordination number or facets (Scheme 2). Oxidation states are usually obtained using X-ray photoelectron spectroscopy (XPS) operating in ultra-high vacuum. Crystal structure interrogation requires imaging techniques like TEM at the single particle level. Combining XPS with TEM is usually useful to distinguish between chemical and crystallographic manifestations of particle size, as well as to monitor potential particle size sintering during catalytic reactions. Also in these lines, mathematical algorithms of Hartog and van der Haldeverd can be employed to determine coordination number on the surface for given particle size and crystal symmetry [40], while geometrical models using the Wulff construction can help in predicting the initial equilibrium morphology [41]. Then, XPS could be solely employed to monitor changes in oxidation state for monometallic catalysts providing that particle sizes vary only marginally throughout the system of interest. Narrow particle size distributions (2–10 %) obtainable by colloidal chemistry renders XPS-led structure–function correlations of catalysts possible. Hence, XPS offers a technical means of understanding and controlling surface chemistry and catalysis. This aspect of synchrotron-based APXPS is clearly exemplified in a study of the size-controlled Rh NPs.

2.1 Size-Dependent CO Oxidation Rates for Monometallic Rh NP Catalysts

In this work, size-uniform Rh NPs were synthetically produced in the 2–11 nm size range, and studied during catalytic oxidation of CO [15]. APXPS was performed using 510 eV (Rh 4d) and 735 eV (O 1 s) photons over 2 and 7 nm Rh NPs, representing small and large particle size regimes, respectively (Fig. 1). Next, Rh $4d_{5/2}$ and O 1 s core level XPS spectra were recorded under CO/O_2 reaction conditions. Finally, catalytic testing was conducted in parallel to the in situ XPS measurements to determine potential structure–function correlations. It was found that the surface of 2 nm Rh NPs were substantially oxidized (67 %) in 0.20 Torr CO and 0.50 Torr O_2, denoted as O-rich condition, at 200 °C, while 7 nm Rh NPs were comprised of mostly metallic Rh (75 %), as shown in Fig. 1a. The main oxide feature at 308.2 eV was assigned to the oxidized RhO_x. O 1s spectra indicated a feature at 529.3 eV, which was attributed to the lattice oxygen of this

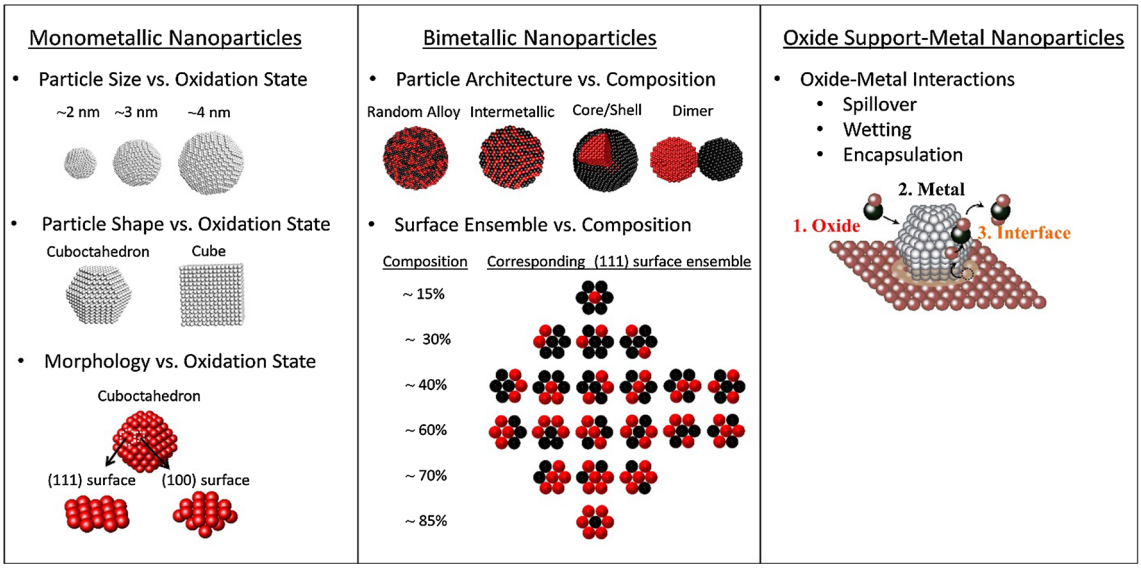

Scheme 2 Common molecular structure factors for monometallic and bimetallic nanoparticles, and oxide support-metal nanoparticle hybrids

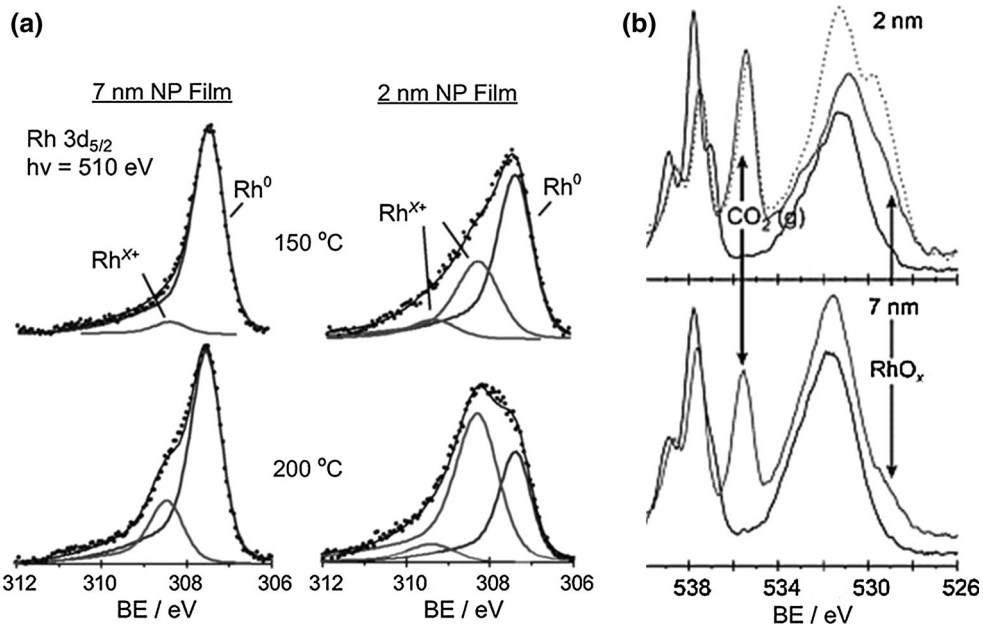

Fig. 1 Rh 3d APXPS spectra of 7 and 2 nm Rh nanoparticle films obtained in 0.7 Torr CO + O_2 (2:5) atmosphere, and at 150 °C and 200 °C (**a**) and O 1 s APXPS spectra measured in 0.7 Torr CO + O_2 (2:5) atmosphere at given temperatures (**b**). In **b** *solid curves* were taken at 150 °C, and dashed curves were taken at and above 200 °C. Metallic and oxidized Rh as well as lattice oxide (i.e. RhO_x) and gas phase CO_2 are indicated on the graphs. APXPS indicated that 2 nm Rh NPs were more prone to oxidation in CO + O_2 in the 150–200 °C range [15]

RhO_x present under the CO + O_2 atmosphere in accord with the Rh 4d XPS. O 1 s spectra also revealed CO_2 in the gas phase, which attested to the fact that CO catalytically reacted with O_2 under the conditions (Fig. 1b). Catalytically, 2 nm Rh NPs exhibited sevenfold enhancement in turnovers for the formation of CO_2 relative to 7 nm Rh NPs, measured in 20 Torr CO and 50 Torr O_2. The enhancement was tentatively ascribed to the oxide phase, which was found more abundantly in the smaller Rh NPs (Table 1).

Size-dependence of the CO + O_2 reaction was also reported by Park and co-workers over size-controlled Ru NPs at two uniform particle sizes: 2.8 and 6.8 nm [42]. Ru NPs were subjected to 0.28 Torr CO + O_2 (2:5) in the 100–200 °C range, while monitoring Ru 3d (and 4p) and O 1 s APXPS spectra. It was found that 2.8 nm Ru had a higher surface fraction of the RuO_2 phase, which the authors identified as catalytically inhibiting for the oxidation of CO, than 6.8 nm Ru across the whole temperature range studied (Table 1).

Table 1 Summary of the APXPS and catalytic screening studies on monometallic Rh [15] and Ru [42] NPs

Monometallic system	Particle sizes evaluated	APXPS pressure & temperature conditions	Catalytic reaction conditions	Materials & catalytic properties correlated via APXPS
Rh	2 & 7 nm	0.28 Torr of CO + O_2 (2:5) in the 150–200 °C range	70 Torr CO + O_2 (2:5) at 200 °C	Enhanced CO oxidation rates for 2 nm Rh NPs with mostly oxidized Rh than 7 nm Rh NP with mostly metallic Rh
Ru	2.8 & 6.8 nm	0.28 Torr of CO + O_2 (2:5) in the 150–200 °C range	70 Torr CO + O_2 (2:5) at 200 °C	Enhanced activity for metallic Ru (6.8 nm Ru NPs) than oxidized Ru (2.8 nm Ru NPs)

3 APXPS Studies on Bimetallic NP Catalysts

It is a common practice in catalysis that solid solutions or mixtures of metals are employed as catalysts to promote catalytic activity and/or selectivity. Addition of a second metal introduces other molecular factors such as surface ensemble and particle architecture, which are not considered for the monometallic case, as shown in Scheme 2. Surface ensemble determines the arrangement of metal atoms on a unit cell basis, and has promotional or (deliberate) inhibitory impacts on catalysis. Particle architecture results from the intra-particle arrangement of any two metals, and can be considered as bulk ensemble. Likewise, it profoundly affects catalysis through geometric and/or electronic effects [43, 44].

Possible particle architectures are infinitely many, and are, in principle, independent of particle size and shape. The most common particle architectures are alloy and core/shell (Scheme 2). Alloy particles can be constructed by an intra-particle arrangement of metal atoms via either ordered or random disordered fashion. The ordered alloy particles are sometimes called intermetallic. In the case of core/shell particles, as the name implies, one metal is trapped inside the particle core while other metal forms shell(s) around it. Core sizes and shell thicknesses are variables that depend on the mixing composition of any two metals. For one particular case of core/shell particles, where core is covered by a single layer of shell at monolayer coverage, near-surface-alloy term is assumed, and widely used [45, 46]. Both thermodynamic and kinetic factors are in play for the establishment of surface ensemble and particle architecture. Surface free energy and lattice energy, also known as cohesive energy, counteract each other to determine the thermodynamically most stable bimetallic configuration. That is, the shell ensemble with the lowest surface free energy and the bulk composition with the largest lattice energy. Miscibility of any two metals is determined as a function of bulk composition, and is predictable by thermodynamic binary phase diagrams for a number of solid solutions. It should, however, be noted that bimetallic nanoparticles prepared via colloidal chemistry are kinetically-trapped under synthetic reaction conditions, and often exhibit size dependent phase behaviors [47]. As a result, it is difficult to predict surface ensemble or particle architecture. Furthermore, reactive gas atmospheres (or liquid media) and thermal effects act upon bimetallic nanoparticles to alter their surface properties. This so-called chemical pumping is the source of adsorbate-induced restructuring of catalysts [48], and thus can be captured in situ using APXPS.

XPS measures the composition at or near surface regions. Mean free paths of photoelectrons reach a minimum of 5–7 Å in the 100–150 eV range, and run 2–3 layers down from the topmost surface. Therefore, XPS using energy tunable synchrotron X-ray sources, allows for depth analysis of catalysts. It is this three-dimensional profiling that makes synchrotron APXPS such a powerful technique in investigating bimetallic catalysts. To this end, APXPS spectra are normalized for the photon flux and photoelectron MFPs of the respective elements. XPS contains the information of ensemble at near surface regions, however, lacks the microscopic details of the spatially-averaged ensemble. However, it is, in principle, possible to determine particle architecture by scanning across photoelectron energies (i.e. depth-profiling). This is very attractive for exploring intra-particle compositional changes of size-uniform bimetallic nanoparticles. In this section, APXPS monitoring of the reversible core/shell restructuring will be first illustrated over a bimetallic PdRh (two 4d transition metals) NP system under oxidizing (NO) and reducing (CO or CO + NO) atmospheres. Next, surface segregation of bimetallic CoCu (two 3d transition metals) NP systems mediated by hydrogen gas will be explained. Finally, AuPd (5d and 4d transition metals) and CoPt (5d and 3d transition metals) NP systems will be discussed to demonstrate the APXPS technique as an in situ probe of surface composition under catalytic CO oxidation conditions.

3.1 Reversible Surface Restructuring of Bimetallic PdRh NPs

For the study of PdRh NP system, 10 nm nanoparticles with nominal 50:50 compositions, denoted as $Pd_{0.5}Rh_{0.5}$, were synthesized and screened under alternating NO and CO atmospheres in 0.1 Torr and at 300 °C, as highlighted in Fig. 2 [48, 49]. Photon energies were tuned such as to give photoelectron kinetic energies of 310, 510 and 1150 eV for both Rh and Pd 4d core levels. Mean free paths of the selected photoelectrons were ~7, ~11 and ~16 Å, respectively, so that different depths into particle cores could be probed. It was found using APXPS that the as-synthesized $Pd_{0.5}Rh_{05}$ NPs, measured in vacuum and at 25 °C, had Rh-rich surfaces (>90 % at 7 Å), while sub-surface regions at ~16 Å already had bulk composition (i.e. 50:50), as shown in Fig. 2a. Similarly, scanning transmission electron microscopy coupled with energy dispersive spectroscopy, measured in vacuum and at single particle level, indicated that $Pd_{0.5}Rh_{05}$ NPs adopted core/shell architectures with Pd-rich cores and Rh-rich shells. When exposed to 0.10 Torr NO at 300 °C, surface regions remained Rh-rich, but, both metals were oxidized, with >90 % RhO_x and 70 % PdO_x measured by APXPS. While maintaining the temperature, first NO was evacuated and then 0.1 Torr NO + CO (1:1) was introduced to the APXPS chamber. In 0.10 Torr NO + CO (1:1) atmosphere, Pd segregated from sub-surface regions to the surface (i.e. 7 Å). This CO-induced segregation transformed the surface to bulk composition (i.e. 50:50 alloy). In an NO atmosphere, Rh diffused back to the surface, now 70 %, and was oxidized to RhO_x (90 %). Upon switching between NO + CO and NO atmospheres, $Rh_{0.5}Pd_{0.5}$ NPs were reversibly cycled between oxidized Rh-rich (>90 %) surfaces and mostly metallic 50:50 alloy surfaces, as shown in Fig. 2b. The observed phenomena were steadily accounted for by the lower surface free energy of metallic Pd relative to metallic Rh in reducing CO gas, and the higher formation enthalpy, or temperature of sublimation, of Rh_2O_3 in the strongly oxidizing NO gas. Bimetallic RhPd NPs synthesized at different bulk compositions, 20:80 Pd-rich and 80:20 Rh-rich, exhibited similar results, which unequivocally showed surface dynamics of bimetallic nanoparticles in reactive gas environments. Compared to bulk RhPd crystal, 15 nm RhPd particles exhibited faster diffusion and higher oxidability or reducibility of Rh in both (O_2) oxidizing and (H_2 and CO) reducing atmospheres between 50 and 350 °C [50]. No particle size dependence below 15 nm has been reported to date. However, it was demonstrated over bimetallic $Rh_{0.2}Pt_{0.8}$ NPs, another Rh-based bimetallic system, that surface compositions were identical for 2.5 nm and 6.5 nm particles in H_2 or $H_2 + C_6H_{12}$ (5:1) atmospheres and at 360 °C [51].

3.2 Irreversible Surface Segregation of CuO in Bimetallic CoCu NPs

Bimetallic NP systems that consist of oxyphilic metals like Co and Cu are of general interest to hydrogenation and combustion catalysis because of their rich oxidation–reduction chemistry. It is for this reason they were investigated using APXPS [52, 53]. Truly bimetallic nanoparticles of CoCu were synthesized with 50:50 compositions and 10 nm uniform sizes. For the as-synthesized $Co_{0.5}Cu_{0.5}$ NPs, conventional XPS, measured in vacuum and at 25 °C, indicated surface enrichment (64 %) of Co. Co was found mostly oxidized (a combination of +2 and +3 states with

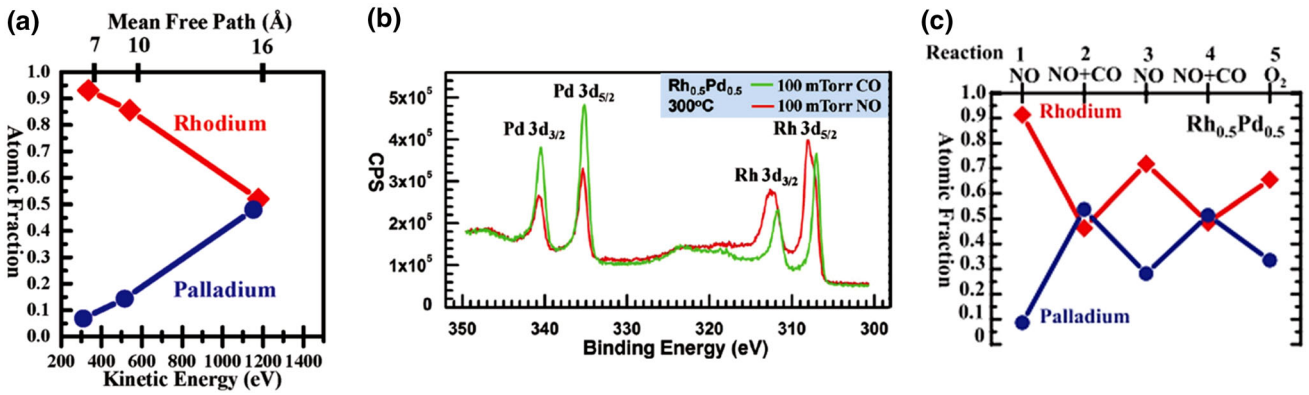

Fig. 2 A plot of atomic fractions of Rh and Pd as a function of photoelectron kinetic energies for the $Rh_{0.5}Pd_{0.5}$ NPs calculated from APXPS spectra measured in vacuum and at 25 °C (**a**). Rh + Pd 3d APXPS spectra of the $Rh_{0.5}Pd_{0.5}$ NPs at 300 °C and in 0.10 Torr of CO (*green*) or NO (*red*) overlapped on top of each other (**b**). Plots of atomic fractions of elements and oxidation states in alternating NO and NO + CO atmospheres and at 300 °C for the $Rh_{0.5}Pd_{0.5}$ NPs (**c**). In vacuum, APXPS indicated Rh enrichment on the particle surfaces. In NO + CO and in the 230–300 °C range, APXPS pointed to reversible surface segregation of Pd, which reinstated the bulk composition. In NO, oxidized Rh-rich surfaces were restored [48, 49]

66 % excess), while Cu was mostly metallic (68 %). STEM/EDS also indicated that individual NPs had Cu-rich cores and Co-rich shells, similar to bimetallic PdRh NPs. APXPS was carried out in reducing (H_2) and oxidizing (O_2) atmospheres using ~310 and ~730 eV photoelectrons, probing about ~8 and ~12 Å of the topmost surface, respectively [52]. 3p shallow core levels were monitored for the in situ XPS studies.

For bimetallic CoCu NPs, APXPS indicated irreversible surface diffusion of Cu and phase segregation of Co and Cu, which is not the case in bimetallic PdRh NPs (Table 2). It was shown in Fig. 3 that surface regions corresponding to a MFP of 8 Å were Co-rich by 70 % in 0.10 Torr H_2 and at 450 °C, while sub-surface regions exhibited bulk composition (i.e. 50:50) under identical conditions [52]. Surface and sub-surface regions were frozen in composition at 200 °C in H_2 and/or CO atmospheres, as illustrated in Fig. 3b for two photon energies. After evacuation, 0.10 Torr O_2 was admitted to the APXPS chamber at 350 °C. O_2 caused complete oxidation of both metal components (Fig. 3a). It was also found in O_2 that surface and sub-surface compositions were totally reversed; that is CuO enriched by 80 %. Compositions on the surface and in the sub-surface regions were once again frozen; even returning to H_2 atmosphere at 450 °C did not induce any significant change on then-Cu segregated surfaces. A post-reduction STEM/EDS investigation of the $Co_{0.5}Cu_{0.5}$ NPs indicated phase segregation of Co and Cu with no apparent mass loss or gain (i.e. no inter-particle diffusion), which then produced segregated dimer NPs (see Fig. 3c).

Carenco et al. studied colloidally-synthesized 22 nm $Co_{0.9}Cu_{0.1}$ NPs using APXPS. Co 2p and Cu 2p core levels were investigated employing 280 eV photoelectrons in reducing (H_2 and/or CO) and oxidizing (O_2) atmospheres [57]. It was reported that CuO was enriched on the surface in 1 Torr O_2 and at 250 °C, while metallic Co migrated back to the surface, restoring the bulk compositions, in 5 Torr H_2 and at 330 °C.

The thermochemical foundations of the observed phenomena warrant further discussion. Co is partially miscible in Cu up to 8 atomic %, and the excess Co is subject to segregation. However, CoO is completely soluble in CuO. These thermodynamic conditions were fundamentally met in the form of core/shell architectures of the as-synthesized NPs, albeit mixtures of metallic and oxide phases, verified by XPS and STEM/EDS in vacuum. Furthermore, APXPS in H_2 atmosphere revealed an increased presence of Co on the surface. In O_2 atmosphere, CuO was enriched on the surface and in the sub-surface regions. In contrary to this observation, as Cu has a lower surface free energy than Co, it was expected that Cu should have populated surfaces more abundantly. Likewise, oxidized NPs should have been more uniform in composition (i.e. $CoCuO_2$). The described aberrations from the bulk thermodynamic behaviors for the CoCu NPs were attributed to a nano-size effect where thermodynamic terms were either altered from

Table 2 Summary of the APXPS studies on PdRh [48, 49], AuPd [54], CoCu [52, 53] and CoPt [55, 56] NPs

Bimetallic system	Particle size & composition evaluated	APXPS conditions	Gas atmospheres & temperature conditions	Materials properties uncovered by APXPS
PdRh	16 nm $Pt_{0.8}Rh_{0.2}$ 16 nm $Pt_{0.5}Rh_{0.5}$ 10 nm $Pt_{0.2}Rh_{0.8}$	Pd & Rh 3d core levels via −310,−510 & −1150 eV photoelectrons	0. 1 Torr of Redox Gases (H_2, O_2, NO & CO) in the 230–300 °C range	Composition independent reversible surface enrichment of RhO_x in (NO) oxidizing conditions above 230 °C
AuPd	9 nm $Au_{0.25}Pd_{0.75}$ 10 nm $Au_{0.5}Pd_{0.5}$ 11 nm $Au_{0.75}Pd_{0.25}$	Au 4f & Pd 3d core levels via −300, −380 & −1400 eV photoelectrons	0.14 Torr of CO + O_2 (2:5) at 200 °C	Composition dependent irreversible surface segregation of Au in CO + O_2 and at 200 °C
CoCu	10 nm$Co_{0.5}Cu_{0.5}$	Co & Cu 3p core levels via −380 & −800 eV photoelectrons	0.1 Torr of Redox Gases (H_2, O_2 & CO). In the 200–450 °C range	Irreversible surface enrichment of CuO, miscible with CoO, in (O_2) oxidizing conditions
CoPt	4 nm $Co_{0.5}Pt_{0.5}$	Co 3p& Pt 4f core levels via −180, −280, −550 & −1400 eV photoelectrons	0.08 & 0.8 Torr of CO + O_2 (1:1.4) at 125 °C	Reversible surface enrichment of Pt, miscible with Co, in (H_2) reducing conditions at 125 °C

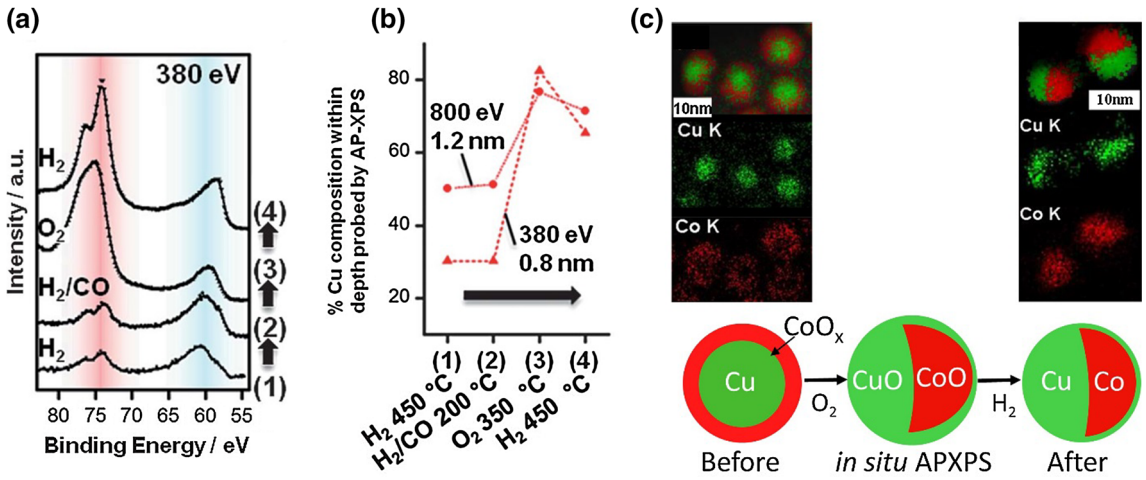

Fig. 3 Co + Cu 3p APXPS spectra of Co and Cu in various reactive gas conditions (**a**) % Cu composition within depth probed by given APXPS conditions. **b** STEM/EDS elemental maps at Co K (*red*) and Cu K (*green*) lines before and after APXPS studies (**c**). Co 3p and Cu 3p APXPS spectra are color coded with *blue* and *red*, respectively, in **a**. *Arrows* in **a**, **b** shows the order that the APXPS spectra were collected. APXPS uncovered irreversible surface segregation and oxidation of CuO in O_2, which was maintained in metallic state upon reduction in H_2. STEM/EDS elemental maps, measured after the fact, revealed phase segregation of Co and Cu following the (O_2) oxidation and (H_2) reduction [52, 53]

their bulk values or somehow counterweighed by kinetic variables due to adsorbate binding.

3.3 Combined APXPS and Catalytic Measurements on Bimetallic NP Systems

In situ knowledge of surface composition is of significance for determining catalytically active phase and ensemble on the surface. APXPS and catalytic reactor measurements when carried out under identical conditions provide valuable mechanistic insight into working catalysts. This strategy was demonstrated for bimetallic NPs of AuPd, PdRh and CoPt during catalytic oxidation of CO, which pointed to unique structure–function correlations for each bimetallic system, and will be discussed below. Catalytic oxidation of CO was chosen to study bimetallic NPs because it is a model reaction with measurable turnovers for low surface area catalysts like two-dimensional Langmuir–Blodgett films of nanoparticles that we often employ in our APXPS studies. Furthermore, its mechanistic and kinetic aspects are well-understood for monometallic transition metals such as Pt, Pd and Rh. Alloying these metals with Au, Cu, Ni and Co have well-documented synergistic effects, albeit no or little mechanistic understanding, and promote catalytic activity orders of magnitude higher than that of the individual members alone. The activity enhancement is usually attributed to geometric, electronic, bi-functional effects, or combinations thereof. XPS was previously employed to try and correlate core level chemical shifts to CO desorption activity on overlayer crystals of transition metals [58–60], which are, in a way, the model counterparts of near surface alloys. Our goal was to obtain surface composition and then to correlate it with turnovers and activation energy to predict the most likely surface ensemble. For this purpose, a reactor chamber where pressure could be varied in the 0.01–1000 Torr range was built, and used for the catalytic measurements of bimetallic (and monometallic parent) catalysts, either nanoparticle films or pelletized powders of supported nanoparticles as used in APXPS measurements. Reaction gases CO, O_2 and CO_2 were continuously leaked from this reactor chamber to a detection chamber, which was held at ultra-high vacuum ($\sim 10^{-10}$ Torr) when the leak valve was closed and at high vacuum ($<10^{-6}$ Torr) during measurements. Mass charges of CO, O_2 and CO_2 were continuously monitored and used to calculate conversions. The examples discussed below give accounts of the structure–function relationships based on the APXPS and the described batch reactor.

3.4 Composition-Dependent Surface Migration of Au in Bimetallic AuPd NPs

A bimetallic AuPd NP system was studied because of its structurally rich phase behavior and well-documented role in CO oxidation reaction [54]. For this purpose, composition-controlled AuPd NPs were synthesized with 25:75 (i.e. Pd-rich), 50:50 and 75:25 (i.e. Au-rich) compositions with narrow size distributions ($\sigma \approx 0.2$) in the 8–11 nm range. APXPS and catalytic measurements, as well as ex situ STEM/EDS, were employed to interrogate the materials aspects of CO oxidation reaction over well-defined AuPd

NPs. 300, 380 and 1400 eV photoelectrons with MFPs of ~6, ~8 and ~15 Å, respectively, were used for the APXPS experiments. First, the particle architecture and surface composition of the as-synthesized NPs were determined using ex situ STEM/EDS and APXPS, both performed in vacuum and at 25 °C. It was found that all AuPd NPs were truly bimetallic and had Au-rich cores and Pd-rich shells (>90 %), as indicated by STEM/EDS. It was also found that particle cores increased in size while Pd shell thicknesses decreased with increasing the Au/Pd ratio, in the order of $Au_{0.25}Pd_{0.75}$ < $Au_{0.5}Pd_{0.5}$ < $Au_{0.75}Pd_{0.25}$ or ~5 < ~10 < ~15 Å, approximated from STEM/EDS and geometric models, for the Pd shells.

APXPS uncovered a composition dependence on surface segregation of Au for the Au-core Pd-shell NPs (Fig. 4a; Table 2). To this end, AuPd NP films were exposed to 0.14 Torr CO + O_2 (2:5) mixture at 200 °C, and changes in Au 4f and Pd 4d core levels monitored over a period of 60 min using 380 eV photoelectrons [54]. It should be noted that the observed changes in XPS spectra usually occurred immediately after the reactive gases were introduced, and no further changes were measured afterwards, indicating that thermodynamic equilibrium has been reached within the time scale of measurements. It was documented that $Au_{0.25}Pd_{0.75}$ and $Au_{0.5}Pd_{0.5}$ NPs with thicker Pd shells remained Pd-rich (>85 %) in the surface regions, while $Au_{0.75}Pd_{0.25}$ NPs with thinner Pd shells were transformed from Pd-rich (~90 %) to Au-rich (~70 %) on the surface (see Fig. 4a). It was also documented that the surface compositions obtained in CO + O_2 atmosphere were final, and maintained in UHV in the 25–200 °C range. Finally, Pd was found to be partially oxidized while Au stayed metallic during catalytic oxidation of CO at 200 °C.

The peculiar observation of one-way restructuring for the $Au_{0.75}Pd_{0.25}$ alone warrants further discussion and some explanation. First, both lattice energy (higher for Pd) and surface free energy (lower for Au) favor Au on the surface and Pd in the bulk. On contrary, enthalpy of adsorption for both CO and O_2 are higher on Pd, which kinetically favor Pd on the surface. In the case of $Au_{0.25}Pd_{0.75}$ and $Au_{0.5}Pd_{0.5}$ NPs kinetic stabilization won over thermodynamic forces to drive Au out of particle cores because Au buried deep underneath thick layers of Pd (>10 Å). However, Au diffused out and covered surfaces for $Au_{0.75}Pd_{0.25}$ NPs as a result that thermodynamic forces could operate effectively across thin Pd shells (~5 Å) screening nearby Au. It

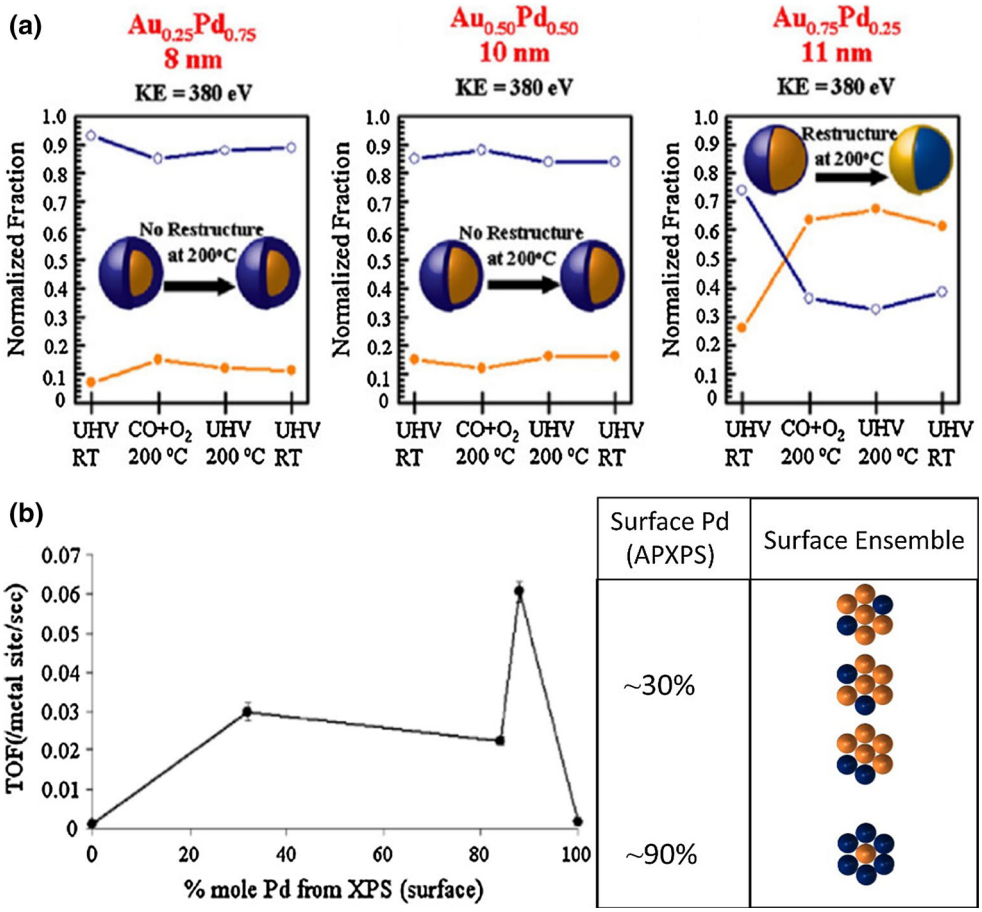

Fig. 4 Atomic fractions of Au (*orange*) and Pd (*blue*) as a function of given reactive gas conditions for $Au_{0.25}Pd_{0.75}$, $Au_{0.5}Pd_{0.5}$, $Au_{0.75}Pd_{0.25}$ NPs (**a**). Plots of turnover frequencies versus % mole Pd from APXPS spectra (**b**). Both turnover frequencies and APXPS spectra were measured in 0.14 Torr of CO + O_2 (2:5) and at 200 °C. Possible (111) surface ensembles are depicted in **b**. APXPS measurements displayed a composition dependence for the core/shell restructuring of bimetallic AuPd nanoparticles. It was also demonstrated using combined APXPS and catalytic measurements that either contagious Pd or Au-rich surface ensembles could give rise to enhancements during catalytic oxidation of CO in 0.14 Torr CO + O_2 and at 200 °C [54]

should be noted that PdRh NPs, another Pd-based bimetallic system, showed surface restructuring in NO and/or CO atmospheres starting at around 230 °C (vide infra). Furthermore, Holgado et al. studied 12 nm AuNi bimetallic NPs via APXPS and using 200 eV and 600 eV photoelectrons, and found Au covered by thick shells of NiO (>1 nm) in vacuum and at 450 °C. They also demonstrated that NP architecture with NiO shells and Au cores were persistent in 0.38 Torr H_2 (or O_2) at 250 °C [61].

3.5 Enhanced CO Oxidation Rates for Au-rich Surface Ensembles in Bimetallic AuPd NP Catalysts

APXPS, combined with catalytic reactivity measurements, demonstrated a correlation between surface ensemble and turnover rates for the catalytic oxidation of CO (Table 3). Catalytically, bimetallic AuPd NPs performed better than the monometallic Pd and Au NPs, which were also synthesized by colloidal chemistry [54]. Turnover frequency (s^{-1}) plotted against surface Pd (atom %) plot showed a synergistic behavior with a maximum for $Au_{0.25}Pd_{0.75}$ NPs (Fig. 4b). A surface ensemble model was derived with the assumptions of (i) a random homogeneous arrangement of Au and Pd atoms, and (ii) a 7-atom unit cell of face centered cubic (111) crystal. By this way, the surface ensemble of $Au_{0.25}Pd_{0.75}$ NPs could be modeled with a single Au atom surrounded with 6 Pd atoms, depicted in Fig. 4b inset. This is exactly the same contiguous Pd surface ensemble proposed in prior studies [62, 63]. Two-fold enhancement for $Au_{0.25}Pd_{0.75}$ NPs relative to $Au_{0.5}Pd_{0.5}$ with apparently identical surface ensemble geometry could then be of electronic origin owing to their different bulk compositions. For comparison, $Au_{0.75}Pd_{0.25}$ NPs should have a contiguous Au ensemble on the surface, yet they are equally as active for the catalytic oxidation of CO as $Au_{0.5}Pd_{0.5}$ NPs. It should be noted that even though the first assumption did not hold and Au unevenly populated the sub-surface layer, the excess Au would have been enough to thwart contiguous Pd. Therefore, our findings using APXPS showed that AuPd with Au-rich surfaces could be equally as effective as that with Pd-rich surfaces in oxidizing CO.

3.6 Surface Enrichment of Pt in Bimetallic CoPt NPs

Alloying Pt with 3d metals like Co is a promising and rewarding approach to alter Pt towards higher catalytic activity and selectivity for a number of reactions of industrial relevance like preferential oxidation of CO in H_2. In this work, 4 nm CoPt alloy NPs, on a gold substrates, were monitored using in situ XAS, APXPS and catalytic reactivity measurements during the $CO + O_2$ (1:1.4) reaction in the 0.08–36 Torr range and at 125 °C [64]. For the APXPS experiments, ~180, ~280 and ~560 eV photoelectrons with corresponding MFPs of ~4, ~6 and ~11 Å were employed. APXPS spectra of Co 3p, Pt 4f and Au 4f, for normalization purposes, were acquired in vacuum as well as 0.10 Torr H_2, 0.08 Torr $CO + O_2$ and 0.80 Torr $CO + O_2$ at 125 °C (Fig. 5a).

APXPS revealed uniform distribution of Co and Pt atoms for the as-synthesized NPs, pointing to an alloy CoPt phase in accord with STEM/EDS. In H_2 atmosphere, Pt was found to have migrated to the surface, forming a thin shell at approximately monolayer coverage (Fig. 5a). In $CO + O_2$ reaction atmospheres, Co replaced Pt on the surface, with gradually more replacement at 0.80 Torr than at 0.08 Torr (Fig. 5b). In situ XAS attested to the oxidation of Co at an onset pressure of about 0.10 Torr $CO + O_2$ at 125 °C. The XAS-probed Co was oxidized partially (40 %) at 0.80 Torr and completely (mixtures of +2 and +3 states) at 36 Torr, suggesting that the surface segregation of Co (i.e. APXPS) was kinetically driven by the oxidation of Co (in situ XAS) [64, 65]. This is also predicted by higher adsorption enthalpy of O_2 on Co than Pt. Metallic Co was restored only partially in $CO + O_2$ atmospheres upon decreasing the total partial pressure back to 0.10 Torr at 125 °C, and completely in reducing H_2 gas at 250 °C.

Papaefthimiou et al. employed APXPS to study bimetallic CoPt deposited on TiO_2 via atomic sputtering

Table 3 Summary of the APXPS and catalytic reactivity measurements on AuPd [54] and CoPt [56] NPs

Bimetallic system	Particle size & composition evaluated	APXPS pressures temperature conditions	Catalytic reaction conditions	Materials & catalytic properties correlated via APXPS
AuPd	9 nm $Au_{0.25}Pd_{0.75}$ 10 nm $Au_{0.5}Pd_{0.5}$ 11 nm $Au_{0.75}Pd_{0.25}$	0.14 Torr of $CO + O_2$ (2:5) at 200 °C	The same as APXPS	Enhanced CO oxidation rates for contiguous Pd or Au-rich surface ensembles
CoPt	4 nm $Co_{0.5}Pt_{0.5}$	0.08–0.8 Torr of $CO + O_2$ (1:1.4)at 125 C	0.01–36 Torr of $CO + O_2$ (1:1.4) at 125 °C	Enhanced activity for surfaces enriched with oxidized Co

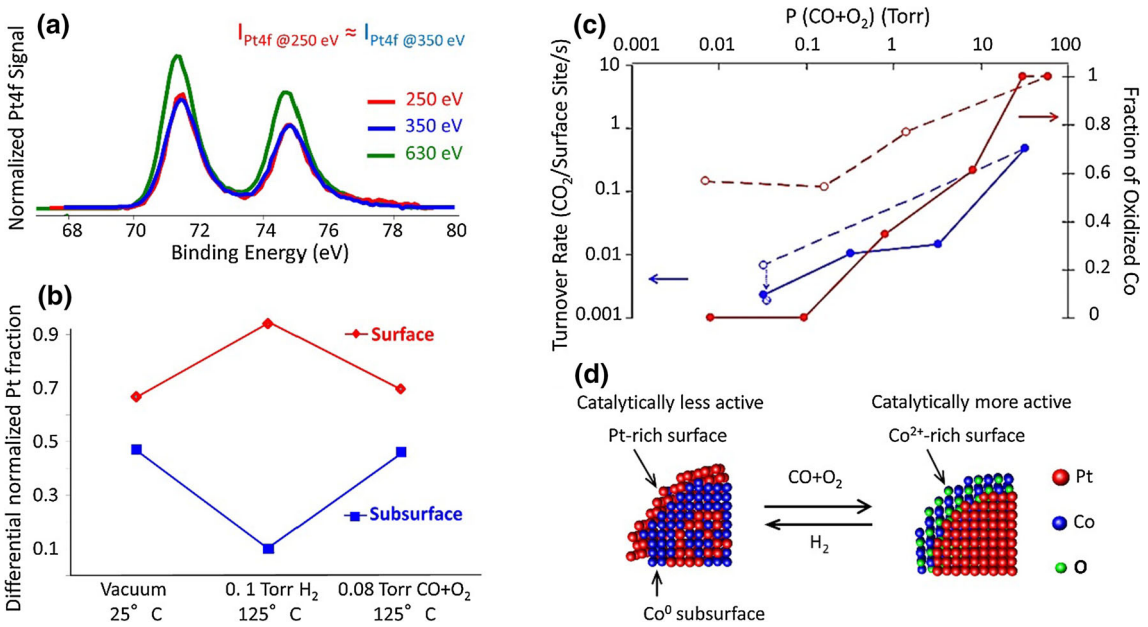

Fig. 5 Normalized Pt 4f APXPS spectra measured in 0.1 Torr H_2 (**a**). Differential normalized Pt fractions for surface and subsurface regions with given depths in various conditions (**b**). Plots of turnover frequencies (*blue*) and oxidized Co fractions from in situ XAS (*red*) as a function of total pressure (i.e. $O_2 + CO$) at 125 °C (**c**). Schematic summarizing the observed structure–function relationship (**d**). In H_2, normalized Pt 4f APXPS spectra using 250 and 350 eV photons overlapped, suggesting depletion of Pt in the subsurface region corresponding to the difference between the two photon energies. It was also suggested by APXPS that Pt, represented with *red* in the schematics, formed approximately a monolayer thick shell on the particle surfaces in H_2. It was shown using in situ XAS, APXPS and catalytic measurements that oxidized Co along with Pt on the surface gave rise to catalytic enhancement during CO oxidation reaction at 125 °C [56]

[66]. They found significant enrichment of Co (80 %) at near surface regions corresponding to 200 eV photoelectrons upon vacuum annealing at ~250 °C. However, they found no changes on the surface elemental make-up in O_2 oxidizing versus H_2 reducing atmospheres at ~230 °C.

3.7 Enhanced CO Oxidation Rates for CoO-Rich Surfaces in Bimetallic CoPt NP Catalysts

Catalytic turnovers for the oxidation of CO were calculated and correlated with the APXPS data (i.e. surface composition), similar to the bimetallic AuPd NPs, and in situ XAS (i.e. oxidation state of Co) results in the 0.08–36 Torr range (Table 3). A linear correlation was found between the total partial pressure and TOFs as compared to a logarithmic relationship expected of purely thermodynamic grounds (Fig. 5c). Given that the oxidation state of Co was exponentially related to the total partial pressure, it was concluded that CoO in contact with Pt was the active catalyst for the oxidation of CO. In accord with this picture, a hysteresis similar to one that was found for the oxidation state of Co was also observed for the catalytic turnovers.

4 APXPS Studies of Binary Metal-Oxide Catalysts

Oxides are often employed as support and/or co-catalyst for metal nanoparticles. SiO_2, Al_2O_3 and MgO are the most commonly used support oxides. They are made of non-reducible, under typical catalytic reaction conditions, cations and usually have the role of providing a large surface area for metal nanoparticles to be loaded in a spatially dispersed manner. By this way, metal centers can be isolated and maintain their physical, chemical and catalytic properties in the course of catalytic reactions. Furthermore, Al_2O_3 and MgO may have acidic and basic surface sites with some mixture of Brönsted and Lewis characters, which are involved directly or indirectly in catalytic processes. SiO_2 is the choice of support in our studies because of its inertness, which allows the metal to be investigated without complications of potential metal-support interactions. Besides their role as co-catalyst, oxides can act in reactive environments to alter the metal morphologically, electronically and chemically. Surface and interface phenomena such as coverage, wetting, mobility and charge transfer have the potential to modify a catalyst towards or away from the sought-after-end products. The phenomena are even more pronounced for oxides

of reducible cations such as TiO_2, CeO_2 and Co_3O_4 which are also known for their defect-induced chemistry.

4.1 Pt-Catalyzed Reduction of CeO_2 in Binary CeO_2/Pt NP Catalyst

Metal-oxide interaction could work in both ways. That is metal modifying oxide surface morphologically, electronically or chemically. Dramatic effects of Pt nanoparticles on the oxidation state and defect chemistry of CeO_2 was documented in H_2 atmospheres using a combination of APXPS, in situ XAS and in situ XRD [67]. In this study, size-uniform 2 nm Pt was loaded on high surface area CeO_2. APXPS was carried out in 0.10 Torr H_2 and in the 75–350 °C range using 380 eV photons, and probing Ce 4d core and Ce 4f valence levels. An empirical methodology developed by Liu and co-workers [68] was employed to calculate fractions of Ce^{4+} and Ce^{3+}.

APXPS revealed that Pt catalyzed the reduction of CeO_2 in H_2 atmosphere (Table 4). A visual inspection of Ce 4d APXPS spectra in Fig. 6a showed evidences of Ce^{3+} formation, starting at 150 °C. Furthermore, Ce 4f APXPS spectra, shown in Fig. 6b, exhibited an inter-band appearing at ~2 eV above Fermi energy in H_2 atmosphere and rising in intensity with increasing temperature. The band falls in the band gap of CeO_2 and thus is assigned to Ce^{3+}. Ce^{3+} concentrations were calculated ~40 % at 350 °C, as plotted in Fig. 6c. It was also shown that Ce^{3+} formed in the bulk and correlated with loss of O^{2-}, which led to the non-stoichiometric CeO_{2-x} $(0.05 < x < 0.1)$ in the 150–350 °C [67]. For pure CeO_2, a steady-state concentration of ~ 5 % was measured for Ce^{3+} in the 350–450 °C range. The activation energy for the reduction of CeO_2 was found ~2.2 eV in the 350–550 °C range, compared to 0.6 eV for the CeO_2/Pt catalyst measured between 75 and 350 °C (Fig. 6c).

Pt-assisted reduction of CeO_2 in H_2 was reversible. In 0.10 m Torr O_2 and at 350 °C, CeO_2 was restored to its oxidized steady-state value of ~95 % Ce^{4+}. It was also found that CeO_2 could be cycled repeatedly between its reduced (40 % Ce^{3+}) and oxidized states (95 % Ce^{4+}), as shown in Fig. 6d. The fact that only the CeO_2/Pt catalyst, not pure CeO_2, is reduced under identical conditions ruled out any X-ray induced reduction channel previously reported for CeO_2 using laboratory sources. On the light of the APXPS, in situ XAS and in situ XRD results, it was proposed that hydrogen atom spillover from Pt NPs facilitated the reduction of Ce^{4+} to Ce^{3+} via creation of oxygen vacancies [67].

5 Combined APXPS and Catalytic Measurements on Binary Metal-Oxide Catalysts

5.1 Ce Oxidation State Effect during Catalytic Oxidation of CO in Binary CeO_2/Pt NP catalyst

The CeO_2/Pt catalyst was investigated using APXPS, in situ XAS and catalytic measurements under CO + O_2 (2:5), denoted O-rich, and CO + O_2 (5:2), denoted CO-rich, reaction atmospheres at 200 and 250 °C [69]. APXPS, carried out in 0.14 Torr total pressures and at 250 °C, indicated at ~95 and ~85 % Ce^{4+} under O-rich and CO-rich reaction conditions, respectively. Furthermore, Ce^{4+} concentrations in the near surface regions were measured using in situ XAS in 15 Torr total pressures, and found identical to those that were given by the APXPS, suggesting no or little dependence on partial pressures (i.e. low oxygen activity) in the pressure range studied. APXPS and in situ XAS independently showed that CO-rich atmospheres had the reducing effect over CeO_2, possibly promoted at the interface with Pt NPs as occurred in H_2 atmospheres (see Fig. 7a, b).

Catalytic measurements, performed in 140 Torr total pressures, indicated nearly two orders of magnitude enhancement under CO-rich reaction conditions for the CeO_2/Pt than pure Pt NPs and CeO_2 separately (Fig. 7c) [69]. The enhancement was tentatively registered to the

Table 4 Summary of the APXPS studies on CeO_2/Pt [67] and TiO_2/Co [23] catalysts

Oxide-metal system	Particle size evaluated	APXPS conditions	Gas atmospheres & temperature conditions	Materials properties uncovered via APXPS
CeO_2/Pt	2.5 nm Pt NPs supported on porous CeO_2	Pt 4f & Ce 3d core levels, & Ce 4f valence states via ~250 eV photoelectrons	0.1 Torr of H_2 or O_2 in the 150–550 °C range	Enhanced (H_2) reducibility of CeO_2 support assisted by Pt; lowered activation energy for (H_2) reduction of CeO_2/Pt compared to pure CeO_2
TiO_2/Co	10 nm Co NPs supported on porous TiO_2	Ti 2p & Co 2p core levels via −150 eV photoelectrons	0.08–0.8 Torr of CO + O_2 (1:1.4) at 125 °C	Partial encapsulation of metallic Co by TiO_2 support in H_2 and at 450 °C; improved wetting of TiO_2 support by oxidized Co in H_2 and at 250 °C

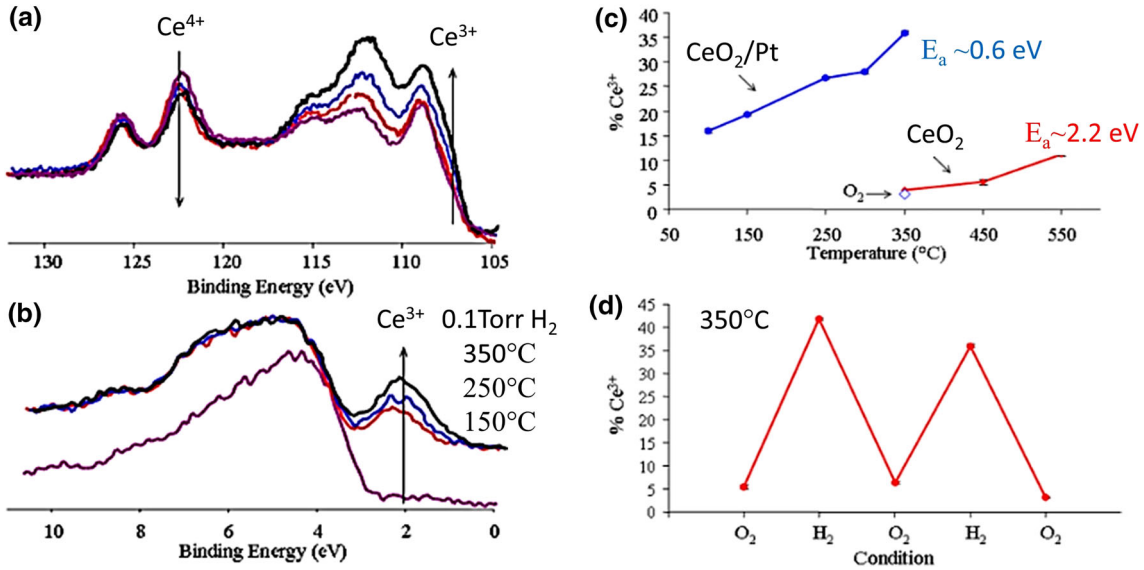

Fig. 6 Ce 4d core level APXPS spectra for CeO_2/Pt catalyst obtained in various reducing (H_2) and oxidizing (O_2) conditions (**a**). Ce 4f valence band APXPS spectra obtained for CeO_2/Pt catalyst in various conditions (**b**). Plots of % Ce^{3+} in 0.10 Torr H_2, calculated from APXPS spectra, in pure CeO_2 (*red*) and CeO_2/Pt (*blue*) catalyst as a function of temperature (**c**). % Ce^{3+} at 350 °C versus alternating O_2 and H_2 atmospheres (**d**). *Blue diamond marker* in (a) indicates % Ce^{3+} in 0.10 m Torr O_2. *Arrows* in **a** show relative changes in Ce^{3+} and Ce^{4+}. *Arrow* in **b** indicated Ce^{3+} inter-band position in H_2. Normalized Ce 4d APXPS spectra, stacked for comparison, indicated the formation of Ce^{3+} in H_2 and in the 150–350 °C range for the CeO_2/Pt catalyst, whereas pure CeO_2 remained unchanged under identical conditions. Accordingly, Ce^{3+} band appeared in the Ce 4f APXPS spectra. The onset temperature, and the activation energy, for the reduction of CeO_2 was substantially dropped for the CeO_2/Pt catalyst. CeO_2 could be reversibly reduced (or oxidized) in H_2 (or O_2) catalyzed by Pt nanoparticles, indicated by APXPS. APXPS results suggested a Pt-mediated reaction pathway for the reduction of CeO_2 [67]

interfacial sites between metallic Pt and O-defect sites (i.e. 85 % Ce^{4+}) on non-stoichiometric CeO_{2-x} present under the given conditions; and the enhancement factors were ~100 relative to both Pt NPs and Pt-free CeO_2. It is usually proposed that the reaction proceeds through a bi-functional mechanism where CO is adsorbed on metallic Pt, and then reacts with O_2 adsorbed on O-defects at or near the interface with CeO_2.

APXPS showed this might not be the case for the CeO_2/Pt catalyst during catalytic CO oxidation. Under O-rich reaction conditions, the enhancement factor relative to Pt NPs was only ~2 This was because the oxidation of CO over Pt NPs alone was promoted in O-rich reaction conditions, and could compete with that occurred at the interfacial sites. However, TOF in O-rich atmosphere (95 % Ce^{4+}) was still twice as much as that in CO-rich atmosphere (85 % Ce^{4+}) at 250 °C. This result unquestionably indicated that defect sites at the interface of Pt NPs and CeO_2 could not have been responsible for the promotional effect in CO_2 production. It was concluded that near-stoichiometric CeO_2 with ~95 % Ce^{4+}, rather than non-stoichiometric CeO_{2-x} ($x \approx 0.04$) with 85 % Ce^{4+}, in contact with metallic Pt gave rise to the dramatic enhancements in oxidation activity. In support of this, TOFs and Ce^{4+} concentrations were correlated at 200 °C as well: more Ce^{4+} was measured by APXPS in O-rich atmosphere (~90 %) than in CO-rich atmosphere (~80 %), where catalytic turnovers were calculated roughly twice as much for the former, as clearly indicated in Fig. 7b, c.

5.2 Metal-Support Interactions in Binary TiO_2/Co NP Catalyst

When deposited on an oxide support, metal nanoparticles wet the oxide surface. That is, in a way, anchoring their atoms to lattice sites or under-coordinated defects on the oxide. This creates a buried interface between the metal and oxide. In one perspective, a dynamic interplay between the interfacial bonding energy and surface free energies decides to what extent wetting occurs or what morphology the metal assumes. Hemispherical particle morphology, where contact angle is roughly 90°, is estimated from TEM studies, and tentatively assumed for noble metals like Pt. What is the particle morphology for oxyphilic metals like Co? To a first approximation, surface free energy will drop and solubility in oxide support will increase when going from metallic Co to oxidized Co (e.g. CoO) as would happen in net oxidizing reaction atmospheres. APXPS probes changes in surface composition that could lead to

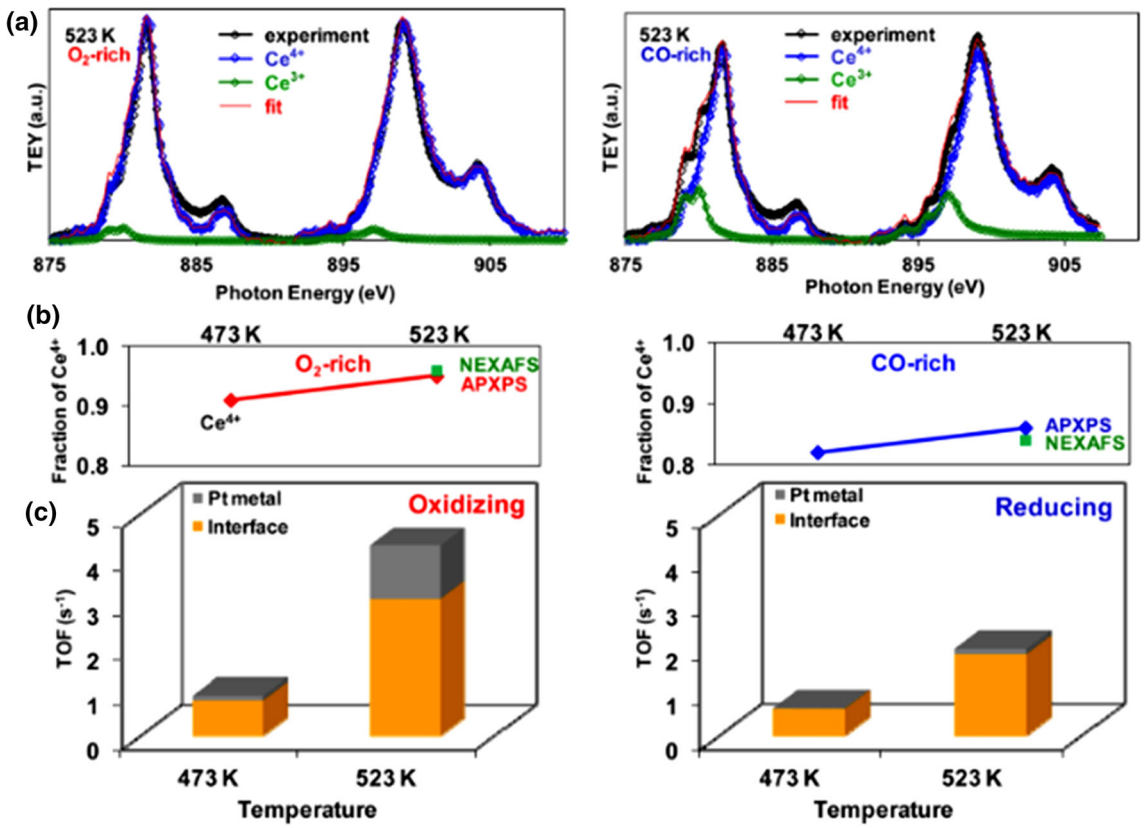

Fig. 7 In situ XAS spectra of CeO_2/Pt catalyst at 250 °C and in 15 Torr of CO/O_2 (2:5) (i.e. O-rich) and CO/O_2 (5:2) i.e. CO-rich) conditions (**a**). Fractions of Ce^{3+} at 200 and 250 °C in O-rich and CO-rich conditions from Ce 3d APXPS and in situ XAS spectra (i.e. NEXAFS) (**b**). *Bar graphs* of turnover frequencies at 200 and 250 °C in O-rich (i.e. oxidizing) and CO-rich (i.e. reducing) conditions (**c**). Least-square fit and fitted Ce^{3+} and Ce^{4+} XAS components are also indicated in **a**. TOFs decomposed into Pt metal and interface (i.e. Pt/CeO_2) are color coded in **c**. Ce^{4+} fractions obtained from APXPS (measured in 0.1 Torr CO + O_2) and in situ XAS (measured in 15 Torr CO + O_2) were almost identical, which suggested no measurable pressure effect in the studied range. Combined in situ XAS, APXPS and catalytic reaction studies indicated a correlation between the fraction of Ce^{4+} sites and catalytic enhancement obtained during CO + O_2 reaction [69]

the understanding and control of such surface phenomena as wetting, clustering and encapsulation for oxide-metal catalysts. APXPS was elemental to demonstrate for 10 nm Co NPs supported on TiO_2 (i.e. TiO_2/Co) that the oxidation state of Co dictated the morphology of Co/TiO_2 interface, which then regulated activity and selectivity during catalytic hydrogenation of CO_2.

In this study, APXPS was used to probe Co 2p and Ti 2p core levels with 180 eV photoelectrons in 0.10 m Torr H_2 (or O_2) in the 250–450 °C range [23]. In H_2, it was observed that Co was almost completely oxidized at 250 °C, and mostly metallic (>50 %) at 450 °C, as shown in Fig. 8a. TiO_2 was also found reduced partially (30 % Ti^{3+}) at 250 °C, and completely in the Ti^{3+} state at 450 °C. Schlögl and co-workers studied 3.5 nm Co NPs using APXPS and 170 eV photoelectrons, and reported an average valence of +2 (i.e. CoO) in 0.15 Torr H_2 and 250 °C, in support of our findings [70]. Furthermore, % surface Co was calculated from APXPS 2p core level spectra. The surface Co was found increased from 25 % in O_2 at 350 °C to 35 % H_2 at 250 °C. In H_2 and at 450 °C, however, the surface Co substantially dropped to 20 %; that was almost half the Co that was measured at 250 °C (Fig. 8b). From these findings, it was proposed that CoO, present in H_2 and at 250 °C wetted TiO_{2-x} ($x \approx 0.2$) surface, increasing its surface area and interfacial contact with TiO_{2-x}. Likewise, metallic Co, present at 450 °C, was encapsulated by the highly non-stoichiometric titania as a result of the lower surface free energy of the latter.

In support of this picture, surface Co measured for the fresh and spent catalyst, before and after catalytic hydrogenation of CO_2, was almost identical to that was measured in situ in O_2 gas (Fig. 8c). It was also apparent from the APXPS analysis that the surface Co almost linearly correlated with the O-defects on titania (i.e. Ti^{3+}); more the O-defects per unit titania, larger the % surface Co was obtained. In their APXPS study of bimetallic CoPt on TiO_2, Papaefthimiou et al. proposed the formation of $Co_xTi_yO_z$

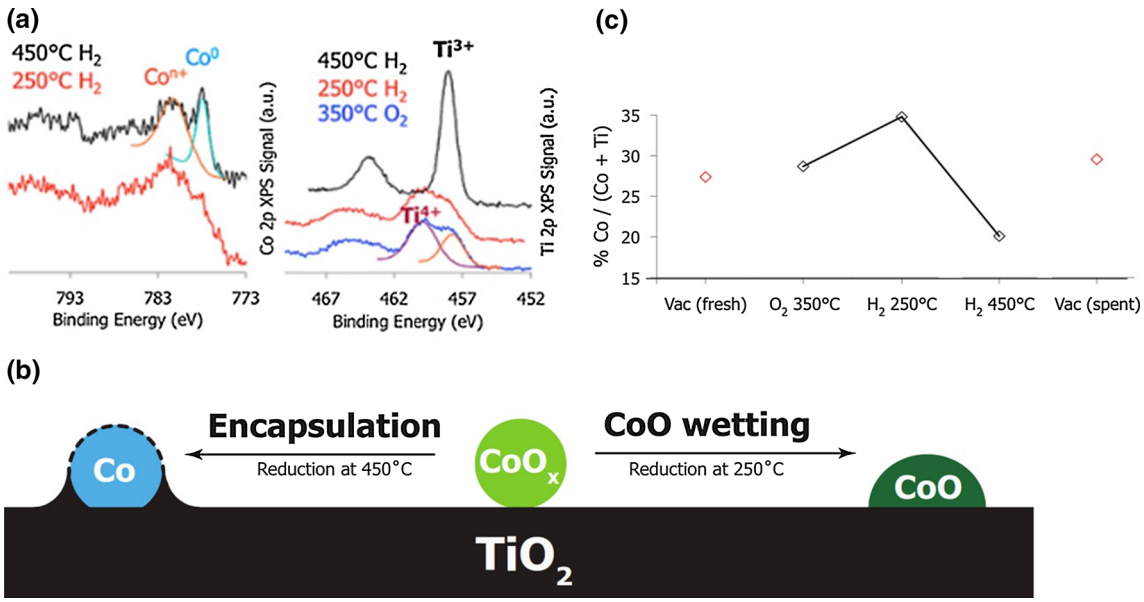

Fig. 8 Co 2p and Ti 2p APXPS spectra for TiO_2/Co (10 nm) catalyst in various conditions (**a**). A plot of % Co/(Co + Ti) form APXPS spectra in various conditions (**b**). Metallic (Co^0) and oxidized (Co^{n+}) Co as well as Ti^{4+} and Ti^{3+} XPS components are indicated in **a**. *Red diamond markers* in **b** indicate % Co/(Co +Ti) obtained from a laboratory XPS with Al K source before (i.e. fresh) and after (i.e. spent) catalysis. Schematic in **c** illustrates encapsulation of metallic Co and CoO wetting of TiO_2, both suggested by APXPS analysis [23]

species at near surface regions in O_2 oxidizing atmospheres at ~230 °C [66].

5.3 Enhanced Methanation Activity for Oxidized Co in Binary TiO_2/Co NP catalyst

For the catalytic hydrogenation of CO_2 in 4 atm H_2 + CO_2 (3:1) ant at 250 °C, 10 nm Co/TiO_2 catalyst exhibited an order of magnitude higher turnovers towards methanation when (H_2) treated at 250 °C compared to (H_2) reduction that took place at 450 °C [23]. In view of the APXPS results, the observed catalytic enhancement could be explained: low temperature H_2 treatment left Co oxidized and titania wetted by CoO, which promoted catalysis via increased surface coverage (i.e. ensemble effect) and interfacial contact area of CoO (i.e. geometric effect), whereas high temperature reduction to metallic state facilitated encapsulation by titania, blocking partially the Co sites available for catalysis.

6 Conclusion

In summary, engineered nanoparticles prepared via colloidal chemistry have unique electronic and catalytic properties, which distinguish them from their bulk and two-dimensional counterparts. When combined with uniform particle sizes and compositions achievable via colloidal synthesis, APXPS paved the way for chemical and elemental investigations of colloidal nanoparticle catalysts under dynamic conditions pertinent to catalytic reactions. By using APXPS, monometallic, bimetallic and binary metal-oxide nanoparticle catalysts were studied in situ and understood structurally and chemically in the molecular level. APXPS-probed restructuring of PdRh NPs and phase segregation of Co and Cu in CoCu NPs were explained in terms of thermodynamic and kinetic factors. Likewise, Pt-catalyzed reduction of CeO_2 and partial encapsulation of metallic Co by TiO_2 in H_2 atmospheres, both uncovered via APXPS, were given as illustrative examples of metal-support interactions. Furthermore, structure–activity relationships were drawn in parallel with catalytic reactor measurements. Particle size dependence of CO oxidation rates for the monometallic Rh and Ru NPs was explained in terms of oxidation states in the 2–7 nm range. Enhanced CO oxidation rates for the bimetallic AuPd and CoPt NPs were, likewise, attributed to their unique elemental and chemical compositions on the near surface regions. By this way, it was demonstrated that in situ studies combining spectroscopy and catalysis are elemental to understanding surface dynamics in relation to reaction turnovers, and further controlling catalytic properties.

7 Future Directions and Challenges

We have identified four key topics that will further benefit catalysis research, which are also elemental to understanding and controlling chemistry at the nanoscale: (1)

APXPS investigation of clusters at the crossroad of molecular and nano sciences, (2) spatially-resolved APXPS capabilities at single particle level in the sub 10 nm, (3) time-resolved APXPS for kinetic studies in the milliseconds and (4) in situ reaction cells with ultra-thin windows. The last three topics require advances in electron detectors, X-ray optics and windows. The first topic calls out for experimentalists to take initiative for the APXPS investigation of metal clusters, either airborne in molecular beams or soft-landed on substrates.

Particle size dependence on catalysis and surface chemistry are apparent for nanoparticles in the 2–7 nm range as in Rh and Ru NP systems. Having one dimensional structural and electronic properties, metal clusters are quite unique compared to their molecular and nano-size counterparts. They are also unique in catalytic applications owing to their uniquely low coordination bonding and localized electronic make-up [71, 72]. Because of their ultra-small sizes ranging from a few atoms like anionic gas phase clusters of Au [73, 74], Ag and Cu [73] to 10 s of atoms like giant ligand passivated Schmid cluster of $Au_{55}(PPh_3)_{12}Cl_6$ [75, 76], they are practically all surface atoms. Furthermore, mass-selection strategies, which allow deposition on any substrate of choice, bring metal clusters even closer to APXPS studies [77, 78]. Therefore, APXPS can be employed to understand chemistry, bonding and electronic structure of clusters, naked or passivated, in the 4–55 atom range under reactive gas atmospheres. Along these lines, empirical correlations and computational algorithms will help to gain insight into initial and final state effects in XPS once an XPS database relating molecular, cluster and nano-size regimes is established.

Single particle sensitivity in APXPS will be revolutionary for studying heterogeneous catalysis and chemical systems. APXPS studies with standing waves, where sub-nanometer depth resolution was achieved over thin films [79], and tender X-ray irradiation, where buried interfaces between metal crystals and oxide crystals or liquids were probed [80], have been recently reported by the prominent groups in the field. Application of these techniques on colloidal nanoparticles and nanocrystals is imminent, and will most definitely benefit the communities of nanotechnology and heterogeneous catalysis. It will also bring advantage to materials characterization in colloidal sciences, where boundary diffusion across buried interfaces could be monitored both intra-particle and inter-particle.

Next, obtaining time transients of surface ad-layer formation and adsorbate diffusion is critical to kinetic evolution of catalysts and mechanistic understanding of catalytic processes. Transient kinetic analysis using flow reactors and mass spectrometry (MS) detection provides chemical information on surface coverage and diffusion of surface species in the sub second time resolution. However, time delays due to gas phase diffusion renders the real-time detection difficult. In the future, APXPS could be used as a primary tool to evaluate transient kinetics of surface coverage while catalytic reaction occurs. Current technology allows APXPS measurements in sub second time scales from a static atmosphere. Once flow reaction cells with ultra-thin windows are realized, transient kinetic analysis with APXPS will bring a whole new experiments into reality.

Graphene, single or multi-layer, is a promising material for fabricating ultra-thin X-ray windows, as it is already demonstrated to store liquids in ultra-high vacuum of TEM [81]. Current graphene technology can produce single layers over Cu foils and multi-layers over Ni foils with small hole sizes (100 s nm) and densities (<3 %). It was also reported that micron size pinholes could be used to detect secondary electrons and ions while maintaining high vacuums better than 10^{-7} Torr [82]. Metal foil could be selectively etched so as to graphene to be exposed. This is an open challenge for researchers of academia and technology alike, which will most definitely carry surface chemistry and catalysis forward. By this way, in situ reaction cells will render possible APXPS measurements in atmospheric pressures and even in condensed matter probing realistic systems hitherto not possible. Homogeneous catalysis, where single-site organometallic catalysts were employed, could be carried out using in situ flow reaction cells. This will allow chemical speciation of metal centers and their ligand shells in short time-scales and with high chemical sensitivity. Therefore, homogeneous catalysis community could be brought closer to the synchrotron sciences.

Acknowledgments Catalysis part of this work was funded by the Chemical Sciences Division (CSD) at the Lawrence Berkeley National Laboratory. Instrument part of this work was funded by the Materials Science Division (MSD) at the Lawrence Berkeley National Laboratory. The research in the CSD and MSD; and the user projects in the Advanced Light Source, Molecular Foundry and National Center for Electron Microscopy were supported by the Director, Office of Energy Research, Office of Basic Energy Sciences of the U.S. Department of Energy under Contract DE-AC02-05CH1123.

References

1. Fellnerfeldegg H, Gelius U, Wannberg B et al (1974) New developments in esca-instrumentation. J Electron Spectrosc Relat Phenom 5:643–689. doi:10.1016/0368-2048(74)85045-0
2. Gelius U, Basilier E, Svensson S et al (1973) A high resolution ESCA instrument with X-ray monochromator for gases and solids. J Electron Spectrosc Relat Phenom 2:405–434. doi:10.1016/0368-2048(73)80056-8
3. Ogletree DF, Bluhm H, Lebedev G et al (2002) A differentially pumped electrostatic lens system for photoemission studies in the millibar range. Rev Sci Instrum 73:3872–3877. doi:10.1063/1.1512336
4. Salmeron M, Schlogl R (2008) Ambient pressure photoelectron spectroscopy: a new tool for surface science and nanotechnology. Surf Sci Rep 63:169–199. doi:10.1016/j.surfrep.2008.01.001

5. Rameshan C, Weilach C, Stadlmayr W et al (2010) Steam reforming of methanol on PdZn near-surface alloys on Pd(111) and Pd foil studied by in situ XPS, LEIS and PM-IRAS. J Catal 276:101–113. doi:10.1016/j.jcat.2010.09.006
6. Rameshan C, Stadlmayr W, Penner S et al (2012) In situ XPS study of methanol reforming on PdGa near-surface intermetallic phases. J Catal 290:126–137. doi:10.1016/j.jcat.2012.03.009
7. Tao F, Dag S, Wang L-W et al (2010) Break-up of stepped platinum catalyst surfaces by high CO coverage. Science 327:850–853. doi:10.1126/science.1182122
8. Zhang C, Grass ME, McDaniel AH et al (2010) Measuring fundamental properties in operating solid oxide electrochemical cells by using in situ X-ray photoelectron spectroscopy. Nat Mater 9:944–949. doi:10.1038/nmat2851
9. Stoltze P, Norskov J (1985) Bridging the pressure gap between ultrahigh-vacuum surface physics and high-pressure catalysis. Phys Rev Lett 55:2502–2505. doi:10.1103/PhysRevLett.55.2502
10. Goodman D (1994) Catalysis—from Single-Crystals to the Real-World. Surf Sci 299:837–848. doi:10.1016/0039-6028(94)90701-3
11. Dellwig T, Rupprechter G, Unterhalt H, Freund HJ (2000) Bridging the pressure and materials gaps: high pressure sum frequency generation study on supported Pd nanoparticles. Phys Rev Lett 85:776–779. doi:10.1103/PhysRevLett.85.776
12. Goodman DW (2003) Model catalysts: from imagining to imaging a working surface. J Catal 216:213–222. doi:10.1016/S0021-9517(02)00112-4
13. Somorjai GA, York RL, Butcher D, Park JY (2007) The evolution of model catalytic systems; studies of structure, bonding and dynamics from single crystal metal surfaces to nanoparticles, and from low pressure (< 10(-3) Torr) to high pressure (> 10(-3) Torr) to liquid interfaces. Phys Chem Chem Phys 9:3500–3513. doi:10.1039/b618805b
14. Choudhary TV, Goodman DW (2005) Catalytically active gold: the role of cluster morphology. Appl Catal -Gen 291:32–36. doi:10.1016/j.apcata.2005.01.049
15. Grass ME, Zhang Y, Butcher DR et al (2008) A reactive oxide overlayer on rhodium nanoparticles during CO oxidation and its size dependence studied by in situ ambient-pressure X-ray photoelectron spectroscopy. Angew Chem-Int Ed 47:8893–8896. doi:10.1002/anie.200803574
16. Cargnello M, Doan-Nguyen VVT, Gordon TR et al (2013) Control of metal nanocrystal size reveals metal-support interface role for ceria catalysts. Science 341:771–773. doi:10.1126/science.1240148
17. Christopher P, Linic S (2010) Shape- and size-specific chemistry of Ag nanostructures in catalytic ethylene epoxidation. Chemcatchem 2:78–83. doi:10.1002/cctc.200900231
18. Alayoglu S, Aliaga C, Sprung C, Somorjai GA (2011) Size and shape dependence on pt nanoparticles for the methylcyclopentane/hydrogen ring opening/ring enlargement reaction. Catal Lett 141:914–924. doi:10.1007/s10562-011-0647-6
19. Pushkarev VV, Musselwhite N, An K et al (2012) High structure sensitivity of vapor-phase furfural decarbonylation/hydrogenation reaction network as a function of size and shape of Pt nanoparticles. Nano Lett 12:5196–5201. doi:10.1021/nl3023127
20. Baker LR, Kennedy G, Van Spronsen M et al (2012) Furfuraldehyde hydrogenation on titanium oxide-supported platinum nanoparticles studied by sum frequency generation vibrational spectroscopy: acid-base catalysis explains the molecular origin of strong metal-support interactions. J Am Chem Soc 134:14208–14216. doi:10.1021/ja306079h
21. Narayanan R, El-Sayed MA (2005) Catalysis with transition metal nanoparticles in colloidal solution: nanoparticle shape dependence and stability. J Phys Chem B 109:12663–12676. doi:10.1021/jp051066p
22. Bezemer GL, Bitter JH, Kuipers H et al (2006) Cobalt particle size effects in the Fischer-Tropsch reaction studied with carbon nanofiber supported catalysts. J Am Chem Soc 128:3956–3964. doi:10.1021/ja058282w
23. Melaet G, Ralston WT, Li C-S et al (2014) Evidence of highly active cobalt oxide catalyst for the fischer-tropsch synthesis and CO_2 hydrogenation. J Am Chem Soc 136:2260–2263. doi:10.1021/ja412447q
24. Iablokov V, Beaumont SK, Alayoglu S et al (2012) Size-controlled model co nanoparticle catalysts for CO_2 hydrogenation: synthesis, characterization, and catalytic reactions. Nano Lett 12:3091–3096. doi:10.1021/nl300973b
25. Kliewer CJ, Aliaga C, Bieri M et al (2010) Furan hydrogenation over Pt(111) and Pt(100) single-crystal surfaces and Pt nanoparticles from 1 to 7 nm: a kinetic and sum frequency generation vibrational spectroscopy study. J Am Chem Soc 132:13088–13095. doi:10.1021/ja105800z
26. Aliaga C, Tsung C-K, Alayoglu S et al (2011) Sum frequency generation vibrational spectroscopy and kinetic study of 2-methylfuran and 2,5-dimethylfuran hydrogenation over 7 nm platinum cubic nanoparticles. J Phys Chem C 115:8104–8109. doi:10.1021/jp111343j
27. Tsung C-K, Kuhn JN, Huang W et al (2009) Sub-10 nm platinum nanocrystals with size and shape control: catalytic study for ethylene and pyrrole hydrogenation. J Am Chem Soc 131:5816–5822. doi:10.1021/ja809936n
28. Crespo-Quesada M, Yarulin A, Jin M et al (2011) Structure sensitivity of alkynol hydrogenation on shape- and size-controlled palladium nanocrystals: which sites are most active and selective? J Am Chem Soc 133:12787–12794. doi:10.1021/ja204557m
29. Bratlie KM, Lee H, Komvopoulos K et al (2007) Platinum nanoparticle shape effects on benzene hydrogenation selectivity. Nano Lett 7:3097–3101. doi:10.1021/nl0716000
30. Pushkarev VV, An K, Alayoglu S et al (2012) Hydrogenation of benzene and toluene over size controlled Pt/SBA-15 catalysts: elucidation of the Pt particle size effect on reaction kinetics. J Catal 292:64–72. doi:10.1016/j.jcat.2012.04.022
31. Somorjai GA (1997) New model catalysts (platinum nanoparticles) and new techniques (SFG and STM) for studies of reaction intermediates and surface restructuring at high pressures during catalytic reactions. Appl Surf Sci 121:1–19. doi:10.1016/S0169-4332(97)00255-9
32. Borodko Y, Lee HS, Joo SH et al (2010) Spectroscopic study of the thermal degradation of PVP-capped Rh and Pt nanoparticles in H-2 and O-2 environments. J Phys Chem C 114:1117–1126. doi:10.1021/jp909008z
33. Menard LD, Xu F, Nuzzo RG, Yang JC (2006) Preparation of TiO_2-supported Au nanoparticle catalysts from a Au-13 cluster precursor: ligand removal using ozone exposure versus a rapid thermal treatment. J Catal 243:64–73. doi:10.1016/j.jcat.2006.07.006
34. Aliaga C, Park JY, Yamada Y et al (2009) Sum frequency generation and catalytic reaction studies of the removal of organic capping agents from Pt nanoparticles by UV-ozone treatment. J Phys Chem C 113:6150–6155. doi:10.1021/jp8108946
35. Lopez-Sanchez JA, Dimitratos N, Hammond C et al (2011) Facile removal of stabilizer-ligands from supported gold nanoparticles. Nat Chem 3:551–556. doi:10.1038/nchem.1066
36. Borodko Y, Humphrey SM, Tilley TD et al (2007) Charge-transfer interaction of poly(vinylpyrrolidone) with platinum and rhodium nanoparticles. J Phys Chem C 111:6288–6295. doi:10.1021/jp068742n
37. Carenco S, Wu C-H, Shavorskiy A et al (2015) Synthesis and structural evolution of nickel-cobalt nanoparticles under H_2 and CO_2. Small. doi:10.1002/smll.201402795

38. La Parola V, Kantcheva M, Milanova M, Venezia AM (2013) Structure control of silica-supported mono and bimetallic Au-Pt catalysts via mercapto capping synthesis. J Catal 298:170–178. doi:10.1016/j.jcat.2012.11.007
39. Schalow T, Brandt B, Starr DE et al (2006) Size-dependent oxidation mechanism of supported Pd nanoparticles. Angew Chem Int Ed 45:3693–3697. doi:10.1002/anie.200504253
40. Vanharde R, Hartog F (1969) Statistics of surface atoms and surface sites on metal crystals. Surf Sci 15:189. doi:10.1016/0039-6028(69)90148-4
41. Herring C (1951) Some theorems on the free energies of crystal surfaces. Phys Rev 82:87–93. doi:10.1103/PhysRev.82.87
42. Qadir K, Joo SH, Mun BS et al (2012) Intrinsic relation between catalytic activity of CO oxidation on Ru nanoparticles and Ru oxides uncovered with ambient pressure XPS. Nano Lett 12:5761–5768. doi:10.1021/nl303072d
43. Hammer B, Norskov JK (1995) Electronic factors determining the reactivity of metal surfaces. Surf Sci 343:211–220. doi:10.1016/0039-6028(96)80007-0
44. Kim D, Resasco J, Yu Y et al (2014) Synergistic geometric and electronic effects for electrochemical reduction of carbon dioxide using gold–copper bimetallic nanoparticles. Nat Commun 5:4948. doi:10.1038/ncomms5948
45. Alayoglu S, Nilekar AU, Mavrikakis M, Eichhorn B (2008) Ru-Pt core-shell nanoparticles for preferential oxidation of carbon monoxide in hydrogen. Nat Mater 7:333–338. doi:10.1038/nmat2156
46. Nilekar AU, Alayoglu S, Eichhorn B, Mavrikakis M (2010) Preferential CO oxidation in hydrogen: reactivity of core-shell nanoparticles. J Am Chem Soc 132:7418–7428. doi:10.1021/ja101108w
47. Hills CW, Mack NH, Nuzzo RG (2003) The size-dependent structural phase behaviors of supported bimetallic (Pt-Ru) nanoparticles. J Phys Chem B 107:2626–2636. doi:10.1021/jp022182k
48. Tao F, Grass ME, Zhang Y et al (2008) Reaction-driven restructuring of Rh-Pd and Pt-Pd core-shell nanoparticles. Science 322:932–934. doi:10.1126/science.1164170
49. Tao F, Grass ME, Zhang Y et al (2010) Evolution of structure and chemistry of bimetallic nanoparticle catalysts under reaction conditions. J Am Chem Soc 132:8697–8703. doi:10.1021/ja101502t
50. Grass ME, Park M, Aksoy F et al (2010) Effect of O-2, CO, and NO on surface segregation in a Rh0.5Pd0.5 bulk crystal and comparison to Rh0.5Pd0.5 nanoparticles. Langmuir 26:16362–16367. doi:10.1021/la101690y
51. Musselwhite N, Alayoglu S, Melaet G et al (2013) Isomerization of n-hexane catalyzed by supported monodisperse PtRh bimetallic nanoparticles. Catal Lett 143:907–911. doi:10.1007/s10562-013-1068-5
52. Beaumont SK, Alayoglu S, Pushkarev VV et al (2013) Exploring surface science and restructuring in reactive atmospheres of colloidally prepared bimetallic CuNi and CuCo nanoparticles on SiO_2 in situ using ambient pressure X-ray photoelectron spectroscopy. Faraday Discuss 162:31–44. doi:10.1039/c2fd20145c
53. Alayoglu S, Beaumont SK, Melaet G et al (2013) Surface composition changes of redox stabilized bimetallic CoCu nanoparticles supported on silica under H-2 and O-2 atmospheres and during reaction between CO_2 and H-2. In situ X-ray spectroscopic characterization. J Phys Chem C 117:21803–21809. doi:10.1021/jp405745n
54. Alayoglu S, Tao F, Altoe V et al (2011) Surface composition and catalytic evolution of Au (x) Pd1-x (x = 0.25, 0.50 and 0.75) nanoparticles under CO/O-2 reaction in torr pressure regime and at 200 A degrees C. Catal Lett 141:633–640. doi:10.1007/s10562-011-0565-7
55. Alayoglu S, Beaumont SK, Zheng F et al (2011) CO_2 hydrogenation studies on Co and CoPt bimetallic nanoparticles under reaction conditions using TEM, XPS and NEXAFS. Top Catal 54:778–785. doi:10.1007/s11244-011-9695-9
56. Zheng F, Alayoglu S, Pushkarev VV et al (2012) In situ study of oxidation states and structure of 4 nm CoPt bimetallic nanoparticles during CO oxidation using X-ray spectroscopies in comparison with reaction turnover frequency. Catal Today 182:54–59. doi:10.1016/j.cattod.2011.10.009
57. Carenco S, Tuxen A, Chintapalli M et al (2013) Dealloying of cobalt from CuCo nanoparticles under syngas exposure. J Phys Chem C 117:6259–6266. doi:10.1021/jp4000297
58. Rodriguez J, Campbell R, Goodman D (1990) Electronic interactions in bimetallic systems—an X-ray photoelectron spectroscopic study. J Phys Chem 94:6936–6939. doi:10.1021/j100381a004
59. Rodriguez J, Campbell R, Goodman D (1991) Electronic interactions in bimetallic systems—Core-level binding-energy shifts. J Vac Sci Technol -Vac Surf Films 9:1698–1702. doi:10.1116/1.577489
60. Rodriguez J, Campbell R, Goodman D (1991) Electron-donor electron-acceptor interactions in bimetallic surfaces—theory and XPS studies. J Phys Chem 95:5716–5719. doi:10.1021/j100168a003
61. Holgado JP, Ternero F, Gonzalez-delaCruz VM, Caballero A (2013) Promotional effect of the base metal on bimetallic Au-Ni/CeO_2 catalysts prepared from core-shell nanoparticles. ACS Catal 3:2169–2180. doi:10.1021/cs400293b
62. Gao F, Wang Y, Goodman DW (2009) CO oxidation over AuPd(100) from ultrahigh vacuum to near-atmospheric pressures: CO adsorption-Induced surface segregation and reaction kinetics. J Phys Chem C 113:14993–15000. doi:10.1021/jp9053132
63. Gao F, Wang Y, Goodman DW (2009) CO oxidation over AuPd(100) from ultrahigh vacuum to near-atmospheric pressures: the critical role of contiguous Pd atoms. J Am Chem Soc 131:5734–5735. doi:10.1021/ja9008437
64. Zheng F, Alayoglu S, Pushkarev V, et al. (2011) Evolution of oxidation state and structure of Co in Co and Co Pt nanoparticles under the reaction environment. Abstr. Pap. Am. Chem. Soc. 241
65. Zheng F, Alayoglu S, Guo J et al (2011) In-situ X-ray absorption study of evolution of oxidation states and structure of cobalt in Co and CoPt bimetallic nanoparticles (4 nm) under reducing (H-2) and oxidizing (O-2) environments. Nano Lett 11:847–853. doi:10.1021/nl104209c
66. Papaefthimiou V, Dintzer T, Lebedeva M et al (2012) Probing metal-support interaction in reactive environments: an in situ study of PtCo bimetallic nanoparticles supported on TiO_2. J Phys Chem C 116:14342–14349. doi:10.1021/jp302320s
67. Alayoglu S, An K, Melaet G et al (2013) Pt-mediated reversible reduction and expansion of CeO_2 in Pt nanoparticle/mesoporous CeO_2 catalyst. In situ X-ray spectroscopy and diffraction studies under redox (H-2 and O-2) atmospheres. J Phys Chem C 117:26608–26616. doi:10.1021/jp407280e
68. Zhang C, Grass ME, Yu Y et al (2012) Multielement activity mapping and potential mapping in solid oxide electrochemical cells through the use of operando XPS. Acs Catal 2:2297–2304. doi:10.1021/cs3004243
69. An K, Alayoglu S, Musselwhite N et al (2013) Enhanced CO oxidation rates at the interface of mesoporous oxides and Pt nanoparticles. J Am Chem Soc 135:16689–16696. doi:10.1021/ja4088743
70. Papaefthimiou V, Dintzer T, Dupuis V et al (2011) Nontrivial redox behavior of nanosized cobalt: new insights from ambient pressure X-ray photoelectron and absorption spectroscopies. ACS Nano 5:2182–2190. doi:10.1021/nn103392x
71. Niu YH, Yeung LK, Crooks RM (2001) Size-selective hydrogenation of olefins by dendrimer-encapsulated palladium

nanoparticles. J Am Chem Soc 123:6840–6846. doi:10.1021/ja0105257
72. Vajda S, Pellin MJ, Greeley JP et al (2009) Subnanometre platinum clusters as highly active and selective catalysts for the oxidative dehydrogenation of propane. Nat Mater 8:213–216. doi:10.1038/NMAT2384
73. Ho J, Ervin K, Lineberger W (1990) Photoelectron-spectroscopy of metal cluster anions—Cun-, Agn-, and Aun-. J Chem Phys 93:6987–7002. doi:10.1063/1.459475
74. Hakkinen H, Yoon B, Landman U et al (2003) On the electronic and atomic structures of small Au-N(-) (N = 4-14) clusters: a photoelectron spectroscopy and density-functional study. J Phys Chem A 107:6168–6175. doi:10.1021/jp035437i
75. Schmid G (1992) Large clusters and colloids—metals in the embryonic state. Chem Rev 92:1709–1727. doi:10.1021/cr00016a002
76. Boyen HG, Kastle G, Weigl F et al (2001) Chemically induced metal-to-insulator transition in Au-55 clusters: effect of stabilizing ligands on the electronic properties of nanoparticles. Phys Rev Lett 87:276401. doi:10.1103/PhysRevLett.87.276401
77. Mao B-H, Chang R, Shi L et al (2014) A near ambient pressure XPS study of subnanometer silver clusters on Al_2O_3 and TiO_2 ultrathin film supports. Phys Chem Chem Phys 16:26645–26652. doi:10.1039/c4cp02325k
78. Roberts FS, Anderson SL, Reber AC, Khanna SN (2015) Initial and final state effects in the ultraviolet and X-ray photoelectron spectroscopy (UPS and XPS) of size-selected Pdn clusters supported on TiO_2(110). J Phys Chem C 119:6033–6046. doi:10.1021/jp512263w
79. Nemšák S, Shavorskiy A, Karslioglu O et al (2014) Concentration and chemical-state profiles at heterogeneous interfaces with sub-nm accuracy from standing-wave ambient-pressure photoemission. Nat Commun. doi:10.1038/ncomms6441
80. Crumlin EJ, Bluhm H, Liu Z (2013) In situ investigation of electrochemical devices using ambient pressure photoelectron spectroscopy. J Electron Spectrosc Relat Phenom 190:84–92. doi:10.1016/j.elspec.2013.03.002
81. Yuk JM, Park J, Ercius P et al (2012) High-resolution EM of colloidal nanocrystal growth using graphene liquid cells. Science 336:61–64. doi:10.1126/science.1217654
82. Liu B, Yu X-Y, Zhu Z et al (2014) In situ chemical probing of the electrode-electrolyte interface by ToF-SIMS. Lab Chip 14:855–859. doi:10.1039/c3lc50971k